






Magnetorotational supernovae: a nucleosynthetic analysis of sophisticated 3D models

M. Reichert ¹★, M. Obergaulinger ¹, M. Á. Aloy ¹, M. Gabler ¹, A. Arcones ^{2,3}
and F. K. Thielemann^{3,4}

¹Departament d'Astronomia i Astrofísica, Universitat de València, Edifici d'Investigació Jeroni Munyoz, C/Dr. Moliner, 50, E-46100 Burjassot (València), Spain

²Institut für Kernphysik, Technische Universität Darmstadt, Schlossgartenstr. 2, D-64289 Darmstadt, Germany

³GSI Helmholtzzentrum für Schwerionenforschung GmbH, Planckstr. 1, D-64291 Darmstadt, Germany

⁴Department of Physics, University of Basel, Klingelbergstrasse 82, CH-4056 Basel, Switzerland

Accepted 2022 October 31. Received 2022 October 11; in original form 2022 June 23

ABSTRACT

Magnetorotational supernovae are a rare type of core-collapse supernovae where the magnetic field and rotation play a central role in the dynamics of the explosion. We present the post-processed nucleosynthesis of state-of-the-art neutrino-MHD supernova models that follow the post explosion evolution for few seconds. We find three different dynamical mechanisms to produce heavy r-process elements: (i) a prompt ejection of matter right after core bounce, (ii) neutron-rich matter that is ejected at late times due to a reconfiguration of the protoneutronstar shape, (iii) small amount of mass ejected with high entropies in the centre of the jet. We investigate total ejecta yields, including the ones of unstable nuclei such as ²⁶Al, ⁴⁴Ti, ⁵⁶Ni, and ⁶⁰Fe. The obtained ⁵⁶Ni masses vary between 0.01–1 M_⊙. The latter maximum is compatible with hypernova observations. Furthermore, all of our models synthesize Zn masses in agreement with observations of old metal-poor stars. We calculate simplified light curves to investigate whether our models can be candidates for superluminous supernovae. The peak luminosities obtained from taking into account only nuclear heating reach up to a few $\sim 10^{43}$ erg s⁻¹. Under certain conditions, we find a significant impact of the ⁶⁶Ni decay chain that can raise the peak luminosity up to ~ 38 per cent compared to models including only the ⁵⁶Ni decay chain. This work reinforces the theoretical evidence on the critical role of magnetorotational supernovae to understand the occurrence of hypernovae, superluminous supernovae, and the synthesis of heavy elements.

Key words: MHD – nuclear reactions, nucleosynthesis, abundances – supernovae: general – stars: Wolf–Rayet.

1 INTRODUCTION

The advent of time-domain astronomy has unveiled a multitude of luminous transients of stellar origin. Among them, supernovae (SNe) are an exceptional example marking the death of massive stars. Besides ordinary SNe releasing energies $\sim 10^{51}$ erg with peak luminosity $\sim 10^{41}$ erg s⁻¹ (Nomoto, Kobayashi & Tominaga 2013), superluminous supernovae (SLSNe; Gal-Yam 2012, 2019; Nicholl et al. 2014; Moriya, Sorokina & Chevalier 2018) and hypernovae (HNe; Iwamoto et al. 1998) excel by their extreme luminosity and energy. Theoretically, these extreme SNe are promising nurseries for the nucleosynthesis of the heaviest chemical elements in the Universe (Nishimura et al. 2006; Nishimura, Takiwaki & Thielemann 2015; Nishimura et al. 2017; Winteler et al. 2012; Reichert et al. 2021a). Furthermore, there is overwhelming observational evidence connecting extreme SNe with other rarer, extremely powerful events, namely, long gamma-ray bursts (IGRB; Woosley & Bloom 2006). Their extreme properties indicate the presence of distinctive and somewhat extraordinary conditions in the stellar progenitors and/or in their circumstellar environment, from which SLSNe and HNe result. Rotation and magnetic fields may be the differential factors

bringing exceptionally powerful or energetic magnetorotationally driven supernovae (MR-SNe). With respect to the expression MR-SNe we include in this category all events where at the end of stellar evolution core collapse with rotation and magnetic fields plays an essential role. This includes events that end with a magnetized neutron star (magnetar) and a specific supernova explosion, as well as events that lead to central black holes (BHs), where the later evolution beyond that point can cause black-hole accretion disc outflows and long-duration gamma-ray bursts. The simulations in the present paper do not yet include the second phase of the evolution of the latter models. In absence of unambiguous detections of MR-SNe only theoretical/numerical models may provide clues on indirect observational signatures beyond their direct detection.

The first theoretical models of MR-SNe date back to 1970s (LeBlanc & Wilson 1970; Bisnovatyi-Kogan, Popov & Samokhin 1976; Meier et al. 1976; Mueller & Hillebrandt 1979; Symbalisty 1984). These pioneering works have been extended and improved during the years reaching some consensus on the fact that MR-SNe tend to produce collimated ejecta (jets) along the stellar rotational axis. In the first 2D axisymmetric hydrodynamical models that became available (e.g. Maeda & Nomoto 2003; Nishimura et al. 2006; Burrows et al. 2007; Tominaga, Umeda & Nomoto 2007) the developing jets were often injected artificially. Until today, there still exist uncertainties in the models, such as the magnitude of

* E-mail: moritz.reichert@uv.es

the magnetic field. This magnetic field can be inherited from the stellar evolution models (e.g. Maeder & Meynet 2003, 2004, 2005; Woosley & Heger 2006; Braithwaite 2008), and further amplified by the magneto-rotational instability (MRI; Obergaulinger et al. 2009; Masada et al. 2012; Mösta et al. 2015; Rembiasz et al. 2016; Nishimura et al. 2017). Currently, the computational frontier include (all or most of) the following elements: three dimensions, general relativity, sophisticated neutrino transport, and detailed microphysics (recent MHD CC-SN simulations are presented in, e.g. Mösta et al. 2015; Müller & Varma 2020; Kuroda et al. 2020; Bugli, Guilet & Obergaulinger 2021; Matsumoto et al. 2022; Varma, Mueller & Schneider 2022, Obergaulinger & Aloy 2021, OA21 hereafter). In parallel to the (magneto-)hydrodynamical modelling, frameworks to investigate nuclear processes were developed. Only more recently, magnetohydrodynamic (MHD) simulations and large nuclear reaction networks were combined to calculate the nucleosynthesis of MR-SNe (Nishimura et al. 2006; Winteler et al. 2012; Nishimura et al. 2015, 2017; Halevi & Mösta 2018; Mösta et al. 2018; Reichert et al. 2021a).

Existing neutrino-driven supernova models can hardly explain the extreme energies and ejected Nickel masses in HNe. However, state-of-the-art 3D MHD simulations usually last a couple of hundreds of milliseconds, resulting into ejected Nickel masses of the order of $10^{-2} M_{\odot}$ (e.g. Winteler et al. 2012; Nishimura et al. 2015, 2017; Mösta et al. 2018; Reichert et al. 2021a), a value much lower than the (model dependent) Nickel ejecta mass in observed HNe (around $\gtrsim 10^{-1} M_{\odot}$ Nomoto et al. 2013). We shall show here that longer simulation times may yield larger Nickel masses (cf. Witt et al. 2021), broadly compatible with observational models.

The high luminosities of SLSNe are hard to explain with the radioactive decay of Nickel only. Thus, two other ingredients could be relevant to explain the observed luminosities. First, a central engine (e.g. a just born magnetar or protomagnetar) may transfer energy to the ejecta (Kasen & Bildsten 2010; Woosley 2010; Dessart et al. 2012; Chatzopoulos et al. 2013; Inserra et al. 2013b; Nicholl et al. 2014, 2015; Metzger et al. 2015; Soker & Gilkis 2017, Obergaulinger & Aloy 2022, OA22 hereafter). Secondly, a potential contribution to the light curve due to interactions with circumstellar matter (e.g. Jerkstrand, Maeda & Kawabata 2020, and references therein). MR-SNe may not yield enough Nickel mass to explain the high luminosity of SLSNe from radioactive sources, but have the merit that they may produce protomagnetars, whose contribution to the peak luminosity can be dominant (e.g. OA22).

Whether MR-SNe are able to provide the necessary conditions for the r-process depends on many processes during the evolution, which can only be addressed with realistic MHD simulations of a variety of progenitors. In 3D simulations a kink instability may develop that will lead to less neutron-rich conditions suppressing the synthesis of heavy nuclei (Mösta et al. 2014, 2018; Kuroda et al. 2020). Whether this happens is still an open question and may depend on physical conditions such as the strength and geometry of the magnetic field as well as numerical ones like the grid resolution. Furthermore, neutrino reactions may lead to more proton-rich conditions (Nishimura et al. 2017; Reichert et al. 2021a).

Here we present the first nucleosynthesis calculations based on 3D simulations with sophisticated neutrino transport. Our results advance our understanding of the following key questions:

(i) Can MR-SNe synthesize the heaviest nuclei known in our Universe? Are the necessary magnetic field configurations and strengths realistic?

(ii) Which radioactive nuclei are synthesized in MR-SNe? How does the explosion energy correlate with the Nickel mass synthesized in this special type of SNe? Can MR-SNe reproduce the typical imprints of elements in old metal-poor stars?

(iii) What are the dominant radioactive nuclei, and what are the resulting peak luminosities?

To answer these questions, we structure the paper as follows: in Section 2 we describe the neutrino-MHD, Eulerian models, and the method to extract Lagrangian tracer particles out of them. Also we report on our procedure to extrapolate in time the SN ejecta conditions to estimate the nucleosynthetic yields on time-scales much longer than the computed ones in our neutrino-MHD simulations. Results are discussed in Section 3, which contains the final ejecta yields (Section 3.1), a brief comparison of the yields of 2D and respective 3D models (Section 3.2), and an analysis of the conditions that are necessary for the r-process (Section 3.3). Additionally, we analyse the yields, conditions, and spatial distribution of radioactive nuclei such as ^{26}Al , ^{44}Ti , ^{56}Ni , ^{60}Fe in Section 3.4. Afterwards in Section 3.5, we investigate the amount of produced Zinc. A simplified light curve model is presented in Section 3.6. Discussions and conclusions are given in Section 4.

2 SIMULATIONS

2.1 Neutrino-MHD models

We investigate four models in full 3D (OA21) and two long-time axisymmetric 2D simulations (Obergaulinger & Aloy 2017, Aloy & Obergaulinger (2021); AO21 hereafter) of the same Wolf-Rayet progenitor star with $35 M_{\odot}$ zero age main sequence mass (ZAMS), a pre-collapse mass of $28.1 M_{\odot}$, and a metallicity of 1/10th of solar metallicity (model 35OC of Woosley & Heger 2006). Hence, the progenitor for all of our models is the same and they only differ in the parametrization and strength of the magnetic field (see magnetic energies in Table 1). All six models were initialized using the rotational profile given by the stellar evolution calculations. In one of the 3D models, model O, we also use the magnetic field given by Woosley & Heger 2006. Also model P in 3D and the equivalent model in 2D (35OC-Rp3) take the estimated magnetic field at the pre-supernova link, but slightly increase the poloidal component strength. In the other three models, the magnetic field is set up as a combination of a large-scale dipole field and a toroidal component, following the prescription of (Suwa et al. 2007). We changed its normalization such as to increase or decrease the field strength w.r.t. the original field obtained by Woosley & Heger 2006. We note that, magnetic fields are only estimated from the saturation of the Tayler-Spruit dynamo process in stellar evolution. Thus, neither the strength, nor the topology of the fields are exactly known. Hence, there is room for some variation of these quantities without modifying any essential property of the pre-supernova model (see Table 1 and Maeder & Meynet 2012; Wheeler, Kagan & Chatzopoulos 2015; Keszthelyi et al. 2019; Müller & Varma 2020; AO21; Varma & Müller 2021; Griffiths et al. 2022). Before core bounce, all models are calculated in 2D axisymmetry and then mapped into full 3D.

Our models O, W, and S are 3D versions of axisymmetric models for which we already computed the nucleosynthetic yields (Reichert et al. 2021a). Model P is another 3D model with an initial field strength between the original and the very strong field of models O and S, respectively (Table 1). We include its axisymmetric version, model 35OC-Rp3, in the present analysis. The 2D equivalent of model S (35OC-Rs) was already presented in Reichert et al. (2021a).

Table 1. Main properties of the simulations. The first two columns list the model name and their spatial dimensionality. The next columns show the pre-collapse energies of the poloidal and toroidal magnetic field components, $E_{\text{mag},0}^{\text{pol,tor}}$, (for comparison, the initial rotational energy of all models is $E_{\text{rot},0} \approx 1.7 \times 10^{50}$ erg). We note that the magnetic energies are integrated over the whole numerical grid. As the outer radii of the 2D and 3D models are slightly different, this also results in a slightly different magnetic energy. The final simulation time after bounce, $t_{\text{f,pb}}$, and the ejected mass, as well as the diagnostic explosion energy¹ at $t = t_{\text{f}}$, the total amount of tracers set and total amount of tracers in which a detailed nucleosynthetic calculation is performed. The last four columns give the number of cells in the radial, θ , and ϕ directions, and the number of neutrino energy bins.

Model	D	$E_{\text{mag},0}^{\text{pol}}$ [erg]	$E_{\text{mag},0}^{\text{tor}}$ [erg]	$t_{\text{f,pb}}$ [s]	Ejected mass [M_{\odot}]	Energy [10^{51} erg]	#Tracers Tot./Calc.	N_r	N_{θ}	N_{ϕ}	$N_{E_{\nu}}$
35OC-Rp3	2	5.0×10^{48}	1.3×10^{49}	8.96	1.58	6.60	41 980/41980	480	128	1	10
35OC-Rs _N	2	7.5×10^{47}	2.6×10^{49}	2.53	2.56	8.96	74 521/3451	480	128	1	8
W	3	1.1×10^{44}	1.3×10^{45}	1.13	0.20	0.52	952 412/2618	300	64	128	10
O	3	2.6×10^{47}	6.6×10^{48}	0.80	0.15	0.49	838 984/2032	300	64	128	10
P	3	2.4×10^{48}	6.6×10^{48}	1.80	0.66	2.06	1286 322/9641	320	64	128	10
S	3	1.1×10^{48}	1.3×10^{49}	1.17	1.61	12.8	1486 316/3459	300	64	128	10

¹The smaller values of the diagnostic explosion energy computed here compared to OA21 arise from a more restrictive criterion for estimating that a computational cell contributes to the ejecta. Here we also request that the radial velocity of an unbound cell must be positive.

There it was run until a final time of $t_{\text{f}} = 0.9$ s. Model 35OC-Rs_N has the same physical initial conditions and a slightly different numerical setup, which allows us to evolve for a much longer time, $t_{\text{f,pb}} = 2.53$ s (AO21).

The models were calculated using the neutrino-MHD code AENUS-ALCAR (Just, Obergaulinger & Janka 2015; Obergaulinger & Aloy 2017). We refer to Obergaulinger & Aloy (2017) and AO21 for a detailed overview of the simulation setup, equation of states (EOS), neutrino transport, and general relativistic corrections on the Newtonian gravitational potential. The resolution differs among our models, having 300–480 zones unevenly spaced (linear and logarithmically) in radial direction, 64–128 zones in θ , and for the case of 3D, 128 zones in ϕ (Table 1). For the neutrino transport M1 scheme (Just et al. 2015), neutrinos are binned into 8–10 logarithmically spaced energy bins. The applied spatial resolution is comparable with the one used in Nishimura et al. (2015) and slightly less compared to the long-time simulations presented in Nakamura, Takiwaki & Kotake (2019). We note that, the numerical grids are not completely analogous among the 2D and 3D models. While the impact of, e.g. grid resolution remains to be explored, the main differences between 2D and 3D models may come from the assumption or relaxation of the artificial condition of axisymmetry.

The models span a wide variety of SN explosion conditions by only varying the magnetic field setup. They include a neutrino-rotational driven case, which behaves in many ways like a classical CC-SN without magnetic fields (model W), a prompt explosion without any stall of the shock (model S and 35OC-Rs_N), models that contain a high entropy outflow (P and 35OC-Rp3), and an intermediate case as inherited by the progenitor magnetic field properties (model O). We shortly summarize the dynamics of the models. Details can be found in Obergaulinger & Aloy (2017), AO21, and OA21.

Model O bears a moderate magnetization, with $b^{\text{pol,tor}} \approx 1.7 \times 10^{10}$; 1.7×10^{11} G for the poloidal and toroidal component at the centre of the star, respectively. Due to these field strengths, the magnetic field has already a dominant influence on the shock revival and the explosion is magnetorotational driven (though neutrinos still have some role). After shock revival, the model develops two jets that reach a radius of $r_{\text{shock}} \sim 8.3 \times 10^3$ km at the end of the simulation (0.8 s post-bounce, Table 1). The morphology of the ejecta (left-hand panels of Fig. 1) corresponds to that of typical bipolar jets, namely a central high-entropy beam or spine, where $Y_e \gtrsim 0.5$, surrounded by a double-lobed cavity. Flanking the jet, we find denser and lower entropy ejecta, where the electron fraction is smaller (with minimum values $Y_e \sim 0.32$). The cavity is limited by the unbound shocked

matter, where, owed to its larger density, the entropy per baryon is lower. The neutron-rich ejecta is more pronounced in the southern (downward) direction (Fig. 1). On the other hand, also slightly neutron-deficient matter ($Y_e > 0.5$) is ejected in the centre of the jet. The entropy is typically higher in the centre of the jet and at the shock front than elsewhere (bottom left-hand panel of Fig. 1). At the end of the simulation the diagnostic energy reached 4.9×10^{50} erg (see footnote 1).

Model W differs from model O in two aspects. First, the original topology of the magnetic field is changed to that of a large scale dipole. Secondly, it has a factor 10 weaker magnetic field, compared to model O ($b^{\text{pol,tor}} \approx 10^{10}$ G). This leads to a neutrino-rotational explosion, as the magnetic field becomes dynamically irrelevant for the shock revival. The model develops rather spherical after shock revival² and the shock expands slower compared to model O. It reaches $\sim 3.7 \times 10^3$ km at 0.8 s post-bounce. In contrast to model O, the model dominantly ejects symmetric and proton-rich material ($Y_e \gtrsim 0.5$). Due to different simulation times, the diagnostic energy at the end of the simulation is slightly higher (5.2×10^{50} erg) compared to model O, even though the explosion occurs less violently.

Model S is the model with the strongest (large-scale, dipolar) magnetic field ($b^{\text{pol,tor}} = 10^{12}$ G). The magnetorotational driven explosion happens promptly after core bounce, without shock stagnation. This leads to a neutron-rich cocoon at the shock front, more pronounced around the southern jet (top right-hand panel of Fig. 1). The expansion of the shock happens extremely quickly, and it reaches already $r_{\text{shock}} \sim 3.0 \times 10^4$ km after 0.8 s post-bounce. The diagnostic energy reaches 1.28×10^{52} erg at the end of the simulation ($t_{\text{f,pb}} = 1.17$ s). Such a large energy is already sufficient to account for the large explosion energies that are observed in HNe. Noteworthy, this model most likely yields an strongly magnetized proto-neutron star as compact remnant.

Model 35OC-Rs_N, the 2D counterpart of the 3D model S, explodes promptly. At first, the shock expands faster than in model S, but later on it falls behind the shock in the latter and reaches $r_s \sim 2.6 \times 10^4$ km at 0.8 s after bounce. Nevertheless, the cocoon around the jet is dominated by even more neutron-rich material, which is also more neutron-rich than the 3D version. The explosion

²We note that this is a major difference compared to the 2D version, model 35OC-Rw, which develops an aspherical explosion (Obergaulinger & Aloy 2017).

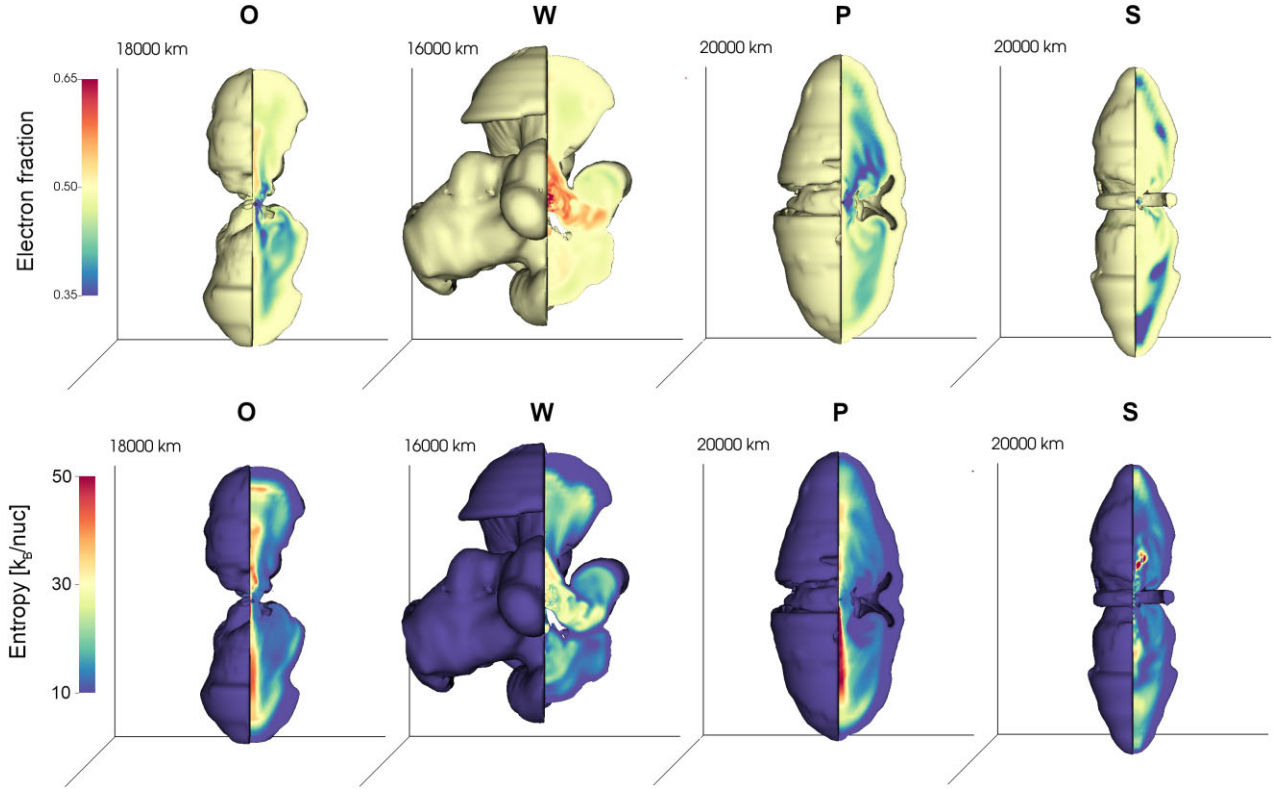


Figure 1. Electron fractions (upper panels) and entropies per baryon (lower panels) of the unbound matter in 3D models. O and W are shown at the final simulation time ($t_{\text{pb}} = 0.80$ s and 1.13 s, respectively) while P and S are shown at earlier times at similar maximum shock radii ($t_{\text{pb}} = 0.63$ s and 0.40 s, respectively).

happens less violently, and the diagnostic energy at the end of the simulation ($t_{\text{f,pb}} = 2.53$ s) is 8.96×10^{51} erg.

Model P has the same toroidal field as model O, but a three times stronger poloidal component. Its magnetization is between models O and S. The shock expands slower compared to models S and 35OC-R_{S_N} and reaches $\sim 1.5 \times 10^4$ km 0.8 s after bounce. Neutron-rich material is ejected within a cone of half-opening angle of $\sim 45^\circ$ around the rotational axis. Small regions in the jet beam reach high entropies of $S > 100 k_{\text{B}}/\text{nuc}$ (k_{B} is the Boltzmann constant). The explosion energy is with 2×10^{51} erg at the end of the simulation ($t_{\text{f,pb}} = 1.8$ s) thus fairly large.

Model 35OC-Rp3 develops very similarly to its 3D version, model P. The shock expands marginally faster in 2D, reaching $r_s \sim 1.9 \times 10^4$ km at 0.8 s after bounce. This model was calculated for a long time ($\simeq 9$ s post bounce), reaching a maximum shock radius of 4.1×10^5 km. The outflow can be moderately neutron-rich ($Y_e \sim 0.25$), though less than in model S. Compared to model P, the maximum ejecta entropy is slightly lower; however, also reaching values $S > 100 k_{\text{B}}/\text{nuc}$ and still larger than the maximum values of all other models. The explosion energy is with 6.6×10^{51} erg at the end of the simulation also fairly high, as expected from the strong magnetization in combination with the long simulation times.

2.2 Tracer particles

The nucleosynthesis calculations are based on Lagrangian tracer particles representing fluid elements of the unbound ejecta. We integrate their equation of motion $\partial_t \vec{X} = \vec{v}(\vec{X})$, where \vec{X} is the position of a tracer particle and \vec{v} the velocity field on the simulation grid. Our strategy differs from similar analyses in that we carry

it out after the MHD models rather than at run-time and perform the integration backward in time instead of forward. This approach has the advantage that it allows us to insert the tracers at the final time of the MHD simulation directly in the gravitationally unbound regions. That way, we achieve a fine coverage of the ejecta without wasting resources on fluid elements that in the end are not ejected. The drawback of the method is that we have to store the velocity field with a sufficiently high cadence (in our case, every 1 ms), thus consuming a large amount of disc space (see Wanajo et al. 2018; Sieverding, Müller & Qian 2020; Witt et al. 2021, for a similar approach). The reliability of this method is tested in Appendix A.

Due to the large computational domain (cf. $r_{\text{max, domain}} \sim 7.7 \times 10^5$ km with a stellar radius $r_* \sim 5.3 \times 10^5$ km), no unbound matter has left the domain at the end of the simulation. Therefore, we do not omit any ejected mass when placing the tracer particles at the last available time in each unbound cell. We say that matter in a computational cell is unbound when two conditions hold: that both the total energy (i.e. internal, kinetic, magnetic, plus gravitational) and the radial velocity are positive. While the second condition (positive radial velocity) is not a necessary condition for unbound ejecta, it filters out fluid elements that fall back onto the central object (see footnote 1). We distribute the total mass of each cell, i.e. the product of its density and volume, $M_{\text{cell}} = \rho_{\text{cell}} V_{\text{cell}}$, flagged as unbound among a number n_{ptc0} of tracer particles placed at random positions in the cell (see e.g. Bovard & Rezzolla 2017, for a discussion of uncertainties arising from different initial placements of tracer particles). By construction, each tracer represents a mass of $M_{\text{ptc0}} = M_{\text{cell}}/n_{\text{ptc0}}$. The number n_{ptc0} can vary between cells. It is determined by two conditions: each unbound cell has to contain

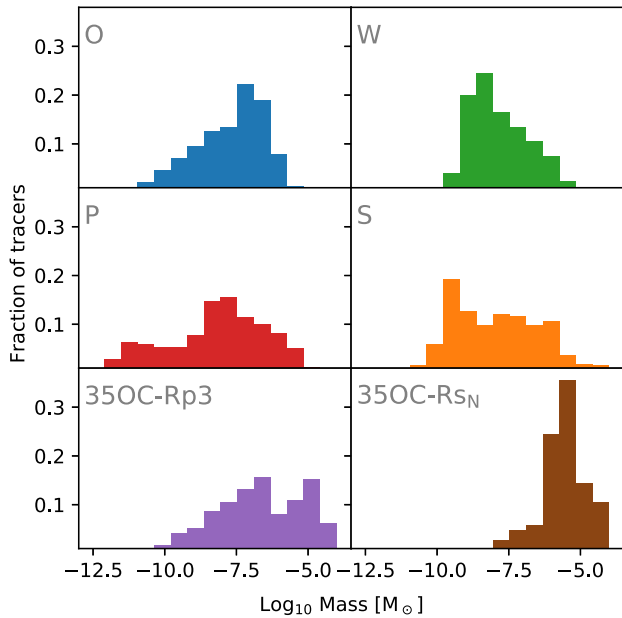


Figure 2. Histogram of the fraction of tracer particles as a function of their masses.

at least two tracers and the mass of each tracer is limited to $M_{\text{ptc}0} \leq 10^{-4} M_{\odot}$. In all models, most of the tracer particles have a mass less than $10^{-6} M_{\odot}$ (Fig. 2). Nishimura et al. (2015) have shown that this resolution is sufficient to obtain a converged result of the nucleosynthesis. For 35OC-Rp3 we set additional tracers into a five degree solid angle around the symmetry axis (i.e. in the jet) to cover better this low density region. The amount of tracer particles is shown in Table 1.

We can vastly reduce the computational cost of the nucleosynthesis calculation by applying a binning procedure and only calculate representative tracers. For this we differentiate between hot ($T_{\text{peak}} \geq 7$ GK) and cold ($T_{\text{peak}} < 7$ GK) tracers. The bins of hot tracers are based on either the electron fraction and entropy at 7 GK. For cold tracers they are based on their peak temperature and density. Our approach works because similar hydrodynamic conditions will end up in similar final abundances (see Appendix B for further details and tests) and we catch all nucleosynthesis relevant conditions. We note that we still use the spatial information of all tracer particles to enable a detailed analysis of the spatial distribution of the elements.

2.3 Nucleosynthesis

To calculate the nucleosynthetic yields, we employ an upgraded version of the nuclear reaction network WINNET (Winteler et al. 2012) as in Reichert et al. (2021a). We included 6545 nuclei up to $Z = 111$. We used reaction rates from the JINA Reaclib database (Cyburt et al. 2010). Furthermore, we include fission reactions as well as fragment distributions from Panov et al. (2005, 2010) and theoretical β -decay rates and electron/positron captures at stellar conditions (Langanke & Martínez-Pinedo 2001). The latter reaction rates are exchanged for experimentally known ones that are included in the JINA Reaclib below the temperature tabulation of Langanke & Martínez-Pinedo (2001) at $T = 0.01$ GK. Neutrino reactions on nucleons are included as in Fröhlich et al. (2006), using the rate tabulation of Langanke & Kolbe (2001).

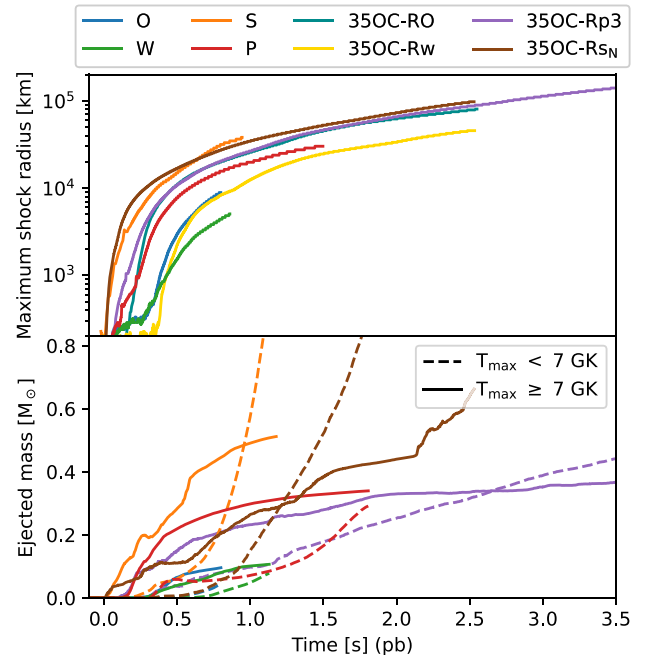


Figure 3. Upper panel: Maximum shock radii of different models versus time post-bounce. In addition to the models discussed within this work, also the 2D versions of model O and W are shown (Obergaullinger & Aloy 2017; Reichert et al. 2021a). It is visible that 2D models tend to develop a larger maximum shock radius at similar times after bounce. Lower panel: Ejected mass of the different models (except models 35OC-RO and 35OC-Rw) as a function of the time post-bounce, distinguishing for each model matter whose maximum temperature is $T_{\text{max}} \geq 7$ GK (solid lines) or $T_{\text{max}} < 7$ GK (dashed lines). The ejected mass of both components is growing until the end of the simulation.

2.4 Finding estimates of the final yields

It is challenging and, to date, not possible to calculate sophisticated 3D neutrino-MHD models for long enough (of the order of few tens of seconds) that nucleosynthesis has effectively finished in a SN explosion. For the time computed in this work, the calculated ejected mass (Table 1) is only a fraction of the total foreseeable ejected mass of the event (see e.g. Harris et al. 2017, for an overview of uncertainties in state-of-the-art nucleosynthesis calculations). To get a more complete picture of the expected total yields of the explosions, it is useful to split the ejected mass into a hot and a cold component, depending on the maximum temperature reached during its evolution, T_{max} (Fig. 3).

Extrapolating the behaviour found in Fig. 3, most of the subsequent additions to the ejecta mass will not reach 7 GK and therefore its composition will be dominated by light elements (i.e. lighter than iron, see also Fig. 4). However, there is also a fraction of hot matter still getting ejected until the end of the simulation even for model 35OC-Rp3, which was simulated up to $t_{f,\text{pb}} = 8.96$ s. Since this hot matter will still contribute significantly to create lighter heavy elements such as Fe, Ni, Zn, or even Sr, we shall estimate the contribution of this fraction of the ejecta too.

In order for unbound matter to attain $T_{\text{max}} \geq 7$ GK, we anticipate two possibilities. When the shock moves outward, the post-shock temperature decreases from above this threshold to lower values. Thus, progenitor matter can only be shock heated to $T_{\text{max}} \geq 7$ GK while the shock is still deep inside the core. At later times, such high temperatures can be achieved if matter gets closer to the hot PNS, from where it may be re-ejected. To estimate the final yields,

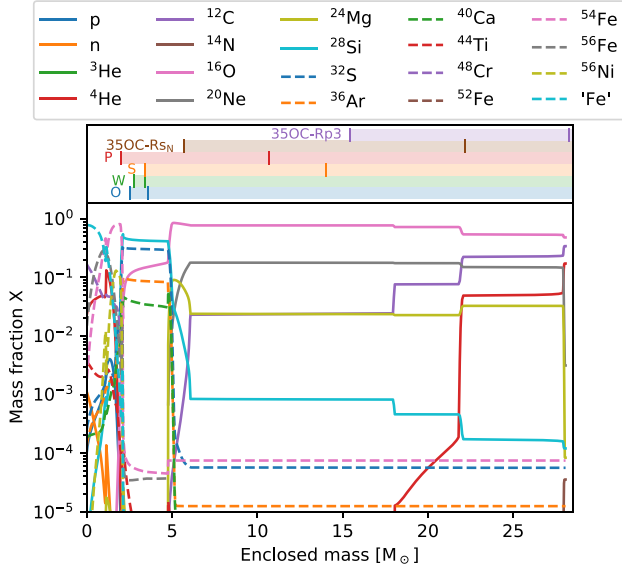


Figure 4. Lower panel: Composition of the progenitor (35OC) from Woosley & Heger (2006). Upper panel: Position of the ejecta outermost and innermost shock wave in the individual models. The two vertical lines indicate the minimum and maximum shock positions at the end of the simulations. Coloured regions ahead of the shock positions correspond to progenitor stellar matter, part of which will be ejected.

it is useful to recall that the progenitor is a rapidly rotating star. Hence, at a finite distance from the centre, the rotating stellar layers possess sufficiently high specific angular momentum to circularize as they hit a centrifugal barrier in their nearly free falling (collapse) trajectory. AO21 estimated this orbit to be located at $M_D \approx 7.5 M_\odot$ and $j \sim 10^{17} \text{ cm}^2 \text{ s}^{-1}$ at the equator (for model 35OC, the progenitor of all models used here). This can be used to find a crude estimate of the outermost mass shell in the star that may contribute to the hot ejecta. Inside M_D , matter has insufficient angular momentum to form an accretion disc. Thus, (a fraction of) these stellar mass shells may be ejected after having fallen close to the central object. The part of the star beyond M_D might fall onto the central object, after assembling an accretion disc. However, our models develop successful (and powerful) SN explosions, which make uncertain what fraction of the mass above M_D may finally end up accreted onto the central object (and hence, not contributing to the ejecta). A more restrictive bound can be obtained by the shock itself. We estimate if the shock is able to drive matter outwards by the mass flux ahead and behind the shock,

$$\dot{M}_{\text{pre}} = 4\pi r^2 \rho_{\text{pre}} v_{r,\text{pre}} \quad \text{and} \quad \dot{M}_{\text{post}} = 4\pi r^2 \rho_{\text{post}} v_{r,\text{post}}, \quad (1)$$

with the density ρ and radial velocity v_r ahead (pre) and behind the shock (post). If $\dot{M}_{\text{pre}} + \dot{M}_{\text{post}} > 0$, matter will be pushed out by the shock, even when it may not get unbound immediately. For each θ and ϕ direction we define three radii, $r_j(\theta, \phi)$, $r_s(\theta, \phi)$, and $r_u(\theta, \phi)$. The radius r_j is defined as the radius at which $j = 10^{17} \text{ cm}^2/\text{s}$ holds and r_s is the shock radius. We define the radius r_u as the radius at which matter will most likely not be able to fall onto the central object, $r_u = \min(r_j, r_s)$. Thus, $r_u = r_j$ if $r_j < r_s$ or if the shock is not able to move matter outwards in the sense as defined above. Otherwise, r_u is set to the shock radius. Summarized, our ejecta is split into several groups:

(i) **Group 1:** Ejecta that are unbound already during the computed neutrino-MHD evolution, i.e. have positive energy and radial velocity.

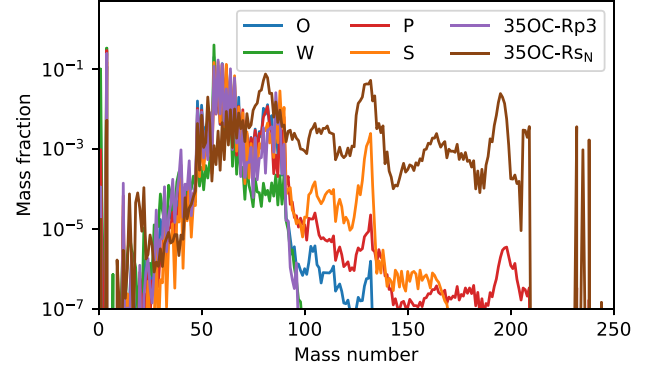


Figure 5. Mass fraction versus mass number for matter ejected during the last 100 ms before the neutrino-MHD simulation ends.

ity. Matter in this group was followed by the tracer particles and constitutes the minimum amount of material that will be ejected.

(ii) **Group 2:** Bound matter (i.e. negative total energy or radial velocity) at the end of the simulation outside of the central object but inside $r < r_u$. We assume that this matter heats up to at least 7 GK, thus contributing to the hot ejecta.

(iii) **Group 3:** Bound matter that is located at radii $r > r_u$ at the final time of the computed neutrino-MHD evolution. We assume that this matter will be shocked and ejected.

(iv) **Group 4:** Stellar wind that was ejected prior to the explosion. The mass is given as the difference between the stellar mass at ZAMS ($35 M_\odot$) and at collapse ($28.1 M_\odot$).

We stress that it is not guaranteed that the entirety of group 2 and group 3 are ejected. A growing mass of the central object could swallow large parts of the mass of the groups, especially if a BH forms. Furthermore, we did not account for the gravitational binding energy of the outer shells from the total energy of each tracer for the definition of group 1 and parts of this group may therefore be not ejected (see Bruenn et al. 2016). This effect may, however, be comparably small. Our extrapolation, assuming that all gas in groups 2 and 3 is ejected, should therefore be seen as a very optimistic case if the entirety of groups get ejected.

For group 1, we already obtained the nuclear composition via the tracer particles in the neutrino-MHD simulation.

To obtain the composition of group 2, we assume that this matter will eventually be ejected similarly to hot matter that got ejected during the last 100 ms before the simulations end (Fig. 5). This assumption obviously has many weaknesses. For example, it cannot be reliably applied to model 35OC-RsN, because the neutron-rich ejecta at the end of the simulation is not expected to continue for a long time (see the r-process pattern in Fig. 5). Additionally, model 35OC-Rp3 develops an almost stable downflow configuration which exists until the end of the simulation. As a result, the estimated amount of significantly heated material is huge ($\approx 7.3 M_\odot$) and, most likely, an artifact of the symmetry assumption of this 2D-axisymmetric model (see also Witt et al. 2021).

For material that is located at radii that exceed r_u (group 3), we calculate the shock temperatures and densities following Nadyozhin & Deupovich (2002). We assume the shock temperature to follow (e.g. Nadyozhin & Deupovich 2002; Woosley, Heger & Weaver 2002)

$$T_s = 2.37 \times 10^9 E_{51}^{0.25} \times R_{09}^{-0.75} \text{ K}, \quad (2)$$

with the final explosion energy E_{51} in units of 10^{51} erg and pre shock radius R_{09} in 10^9 cm. Furthermore, the shock properties evolve

Table 2. Post-shock calibration parameters of the different models. The error is defined as the standard deviation from the parameter from all fitted tracer particles.

Model	ϵ_p	ϵ_T	ϵ_R
W	1.04 ± 0.09	0.40 ± 0.17	0.95 ± 0.30
O	1.14 ± 0.09	1.08 ± 0.33	1.12 ± 0.40
P	0.81 ± 0.14	0.44 ± 0.44	0.42 ± 0.34
S	0.55 ± 0.11	0.19 ± 0.11	0.31 ± 0.20
35OC-Rp3	0.59 ± 0.11	0.15 ± 0.14	0.27 ± 0.19
35OC-RsN	0.54 ± 0.09	0.19 ± 0.40	0.16 ± 0.15

significantly on time-scales (Nadyozhin & Deputovich 2002),

$$t_u = 3.83 \times 10^{-3} \rho_0^{0.5} \times E_{51}^{-0.5} \times R_{09}^{2.5} \text{ s}, \quad (3)$$

where ρ_0 is the density before shock arrival. For a Lagrangian layer crossed by the expanding shock, Nadyozhin & Deputovich (2002) obtained a temperature, density, and radius evolution that follows

$$T(t) = \frac{T_p}{1 + \epsilon_T \times t/t_u}, \quad T_p = \epsilon_p T_s \quad (4)$$

$$\rho(t) = \rho_p \left(\frac{T}{T_p} \right)^3, \quad \rho_p = 7\rho_0 \quad (5)$$

$$R(t) = R_0 \times (1 + \epsilon_r t/t_u), \quad (6)$$

with ϵ_p , ϵ_T , and ϵ_r being parameters that we calibrate for each model individually. Precisely, we fit the evolution of the temperature, density and radial location of each ejected tracer particle that has been shocked by the expanding SN shock during the neutrino-MHD computed time to the functional forms of equations (4)–(6) (the mean value and standard deviation of all fits is given in Table 2). We confirmed that matter is indeed radiation dominated for most of the density range and $\gamma = 4/3$ and consequently $\rho_p = 7\rho_0$ is a reasonable approximation. Furthermore, we tested an extrapolation using $\gamma = 5/3$ and only find minor differences in the final abundances. With these Lagrangian evolutions we account for the mass located outside the shock by calculating a typical evolution for each radius, using the initial composition in mass coordinates of the progenitor. For E_{51} we take the diagnostic explosion energy at the end of the neutrino-MHD simulation as given in Table 1.

To test our extrapolation, we calculated total ejected yields as described above for model 35OC-Rp3 after different times from 1 s to 9 s in 0.5 s steps using the same fitting parameters as in Table 2. For elements dominantly ejected within group 3, namely the α -elements such as ^{16}O , ^{20}Ne , or ^{24}Mg the extrapolated values agree within ~ 30 per cent for all tested times. For extrapolations after 3 s post-bounce, they even agree within ~ 3 per cent. The extrapolated yields of ^{44}Ca and ^{56}Fe that are mainly produced within group 2 agree within a factor of ~ 2 . Heavier elements with $90 \lesssim A \lesssim 130$ are converged within a factor of 10. Again, the estimate gets significantly better for $t > 3$ s after which the extrapolated values agree within a factor of 2. For these heavier elements, we tend to estimate higher ejected masses for extrapolations at earlier times. This is expected as the electron fraction of the ejected matter moves to more symmetric conditions at later simulation times while our estimate is based on the distribution of the last 100 ms. This tends to favor more neutron-rich conditions in the extrapolation. Elements heavier than $A \gtrsim 130$ show a bad agreement within 2 mag only.

We are aware that our estimates are very crude. They are aimed to stress that the amounts of nucleosynthetic yields computed until $t = t_f$ are lower bounds of the final products in our models. Our treatment completely neglects the presence of reverse shocks. Furthermore, the

total yields strongly depend on the final fate of the central object. In the case of models O and W, the PNS may collapse to a BH as this happens in the 2D version of O and even when not happened so far, it is also expected in the 2D version of W (see AO21 for a discussion of BH formation). In this case, a major fraction of the inflowing matter will be accreted by the central BH. Contrary, more material from a later forming accretion disc may get unbound (e.g. by viscous effects) and might also synthesize heavier elements (the ejecta of a so-called collapsar, for which a still ongoing discussion exists; MacFadyen & Woosley 1999; Surman & McLaughlin 2004; McLaughlin & Surman 2005; Surman, McLaughlin & Hix 2006; Fujimoto, Nishimura & Hashimoto 2008; Siegel, Barnes & Metzger 2019; Miller et al. 2020; Siegel et al. 2021; Just et al. 2022a). Within the scope of our work, we can not estimate the conditions of material from a collapsar as detailed simulations would be required.

Nevertheless, our treatment gives a rough estimate of the potential of the models to still synthesize material as, e.g. ^{56}Ni and other unstable isotopes further discussed in Section 3.4. Such an extrapolation is important to shed light into the question whether MR-SNe can be candidates for HNe or SL-SNe.

3 RESULTS

3.1 Ejecta composition

The yields, as shown in the final composition of the ejecta in Fig. 6, vary considerably among our models, with stronger initial magnetic fields leading to heavier elements. The most magnetized models P, 35OC-RsN, 35OC-Rp3, and to some extends also S, synthesize elements up to the third r-process peak ($A \sim 200$), while models with weaker magnetization only reach the second r-process peak (O) or the first peak (W).

Fig. 7 shows the overproduction factor of isotopes, X_*/X_\odot , i.e. the ratio between the mass fraction in one of our models, X_* , and the solar value, X_\odot . The overproduction factor is shown for the lower bound of the ejecta (i.e. group 1, see Section 2.4). Individual isotopes of one element are connected by lines. Positive/negative slopes of the lines indicate that a model favors the production of more neutron-/proton-rich isotopes compared to the Sun. Most models populate more neutron-rich isotopes (e.g. Ti); however, model W is an exception. There, the isotopic ratios are more similar to the sun (i.e. flatter, e.g. Kr). Furthermore, for elements heavier than Sr such as, e.g. Zr, Mo, and Ru more proton-rich isotopes are synthesized for this model. This overproduction factor is caused by more proton-rich conditions compared to the other models (cf. Fig. 1). Complete tables of the ejecta composition can be found in Appendix D.

3.2 Comparison of 2D and 3D models

Based on Fig. 8, we discuss the differences in the nucleosynthesis between 2D and 3D models. Most of our 3D models show a signature of saturation of the explosion energies already by the final simulation times (and note that 3D models are computed for shorter post-bounce times than 2D ones). Contrarily, the explosion energy within the 2D models grows continuously with simulation time. Eventually, we expect that 2D models will reach a higher explosion energy. Model S is an exception to this behaviour as it does not show any saturation in 3D and the explosion energy grows faster than in its 2D counterpart. For a deeper discussion of the impact of the dimensionality on the dynamical evolution, see Obergaulinger & Aloy (2020, 2021), Bugli et al. (2021), and AO21. We want to stress that the differences between 2D and 3D models discussed here are not only influenced

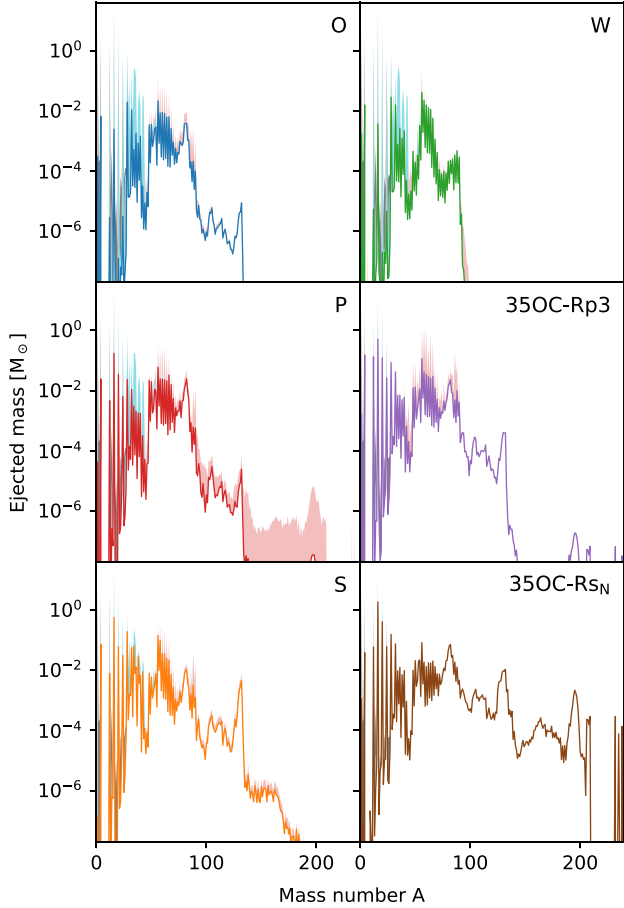


Figure 6. Final ejected masses as a function of mass number for the individual models. Lower lines represent the ejecta mass contained in the Lagrangian tracer particles (group 1, see Section 2.4). Shaded red regions indicate the potential contribution of significantly heated material after the simulation has ended (group 2, except for model 35OC-Rs_N, see text). Shaded cyan regions show the contribution from later shocked material (group 3). The contribution of the stellar wind is indicated as grey region.

by the assumption of axisymmetry, but also by different resolutions in the simulation setups (see Section 2.1). We expect the effects of different resolutions to be relatively minor, but a more detailed study will be necessary in the future.

Within our models, we observe general features in between 2D and 3D models. For instance, 2D models hosts a much more collimated jet cavity compared to 3D models (Fig. 9 and 10). The difference is larger for a weaker magnetization and becomes less for stronger magnetizations. Connected to this, the maximum shock radius develops, as a tendency, faster in 2D (Fig. 3). The ejected mass, however, is lower at times with similar maximum shock radii. Additionally, 2D models seem to produce conditions for a more proton-rich jet. When analysing this phenomena in more detail, we discovered a potential correlation between the shape of the PNS and the proton-rich jet. A more oblate PNS leads to an increased neutrino flux on the rotational axis and, as a consequence, to larger electron fractions. Even though not impossible in full 3D models, this effect is more common and amplified within 2D axisymmetric models (Fig. 10).

The weakly magnetized model W explodes more spherical in 3D compared to its 2D counterpart (Fig. 9). Most strikingly, compared to the 3D model, a lower electron fraction component ($Y_e < 0.5$)

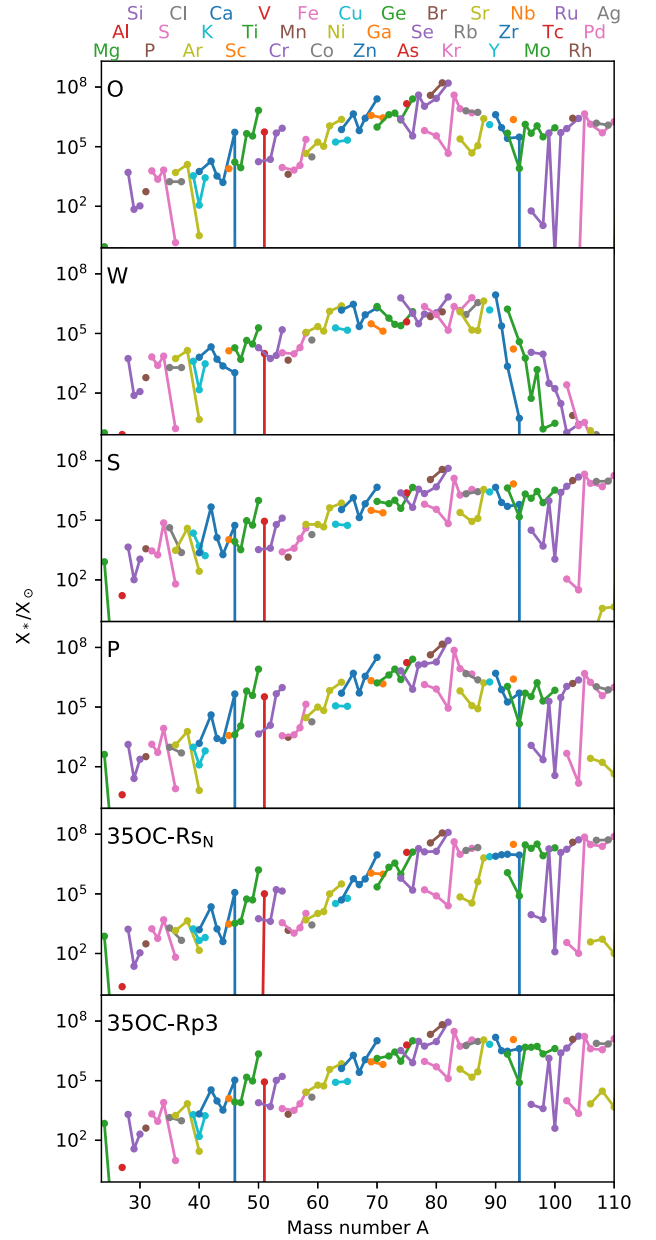


Figure 7. Isotopic ratios relative to the sun for ejecta as obtained from our tracer particles (i.e. group 1, see Section 2.4). Isotopes of the same element are illustrated as a chain of the same colour. Solar values are taken from Lodders, Palme & Gail (2009). The upper labels correspond to the elements represented (according to their atomic number from left to right).

is present. We note that this component is not located in the jet that is in both cases (2D and 3D) proton-rich (see Fig. 10 for a snapshot at similar maximum explosion radii). From a nucleosynthesis perspective, the differences between 2D and 3D are small for elements around iron. However, there are significant differences in the amount of lighter elements ($A \lesssim 40$). The lower yields in 3D are related to two reasons. The first is the shorter evolution time of the 3D model, ending at a final time $t_{f,pb} = 1.13$ s compared to the 2D version ($t_{f,pb} = 2.5$ s), i.e. while the ejection of these elements is still ongoing. A second possible reason are different conditions for explosive nucleosynthesis owing to the different shapes of the shock (left-hand panel of Fig. 9, see also OA21).

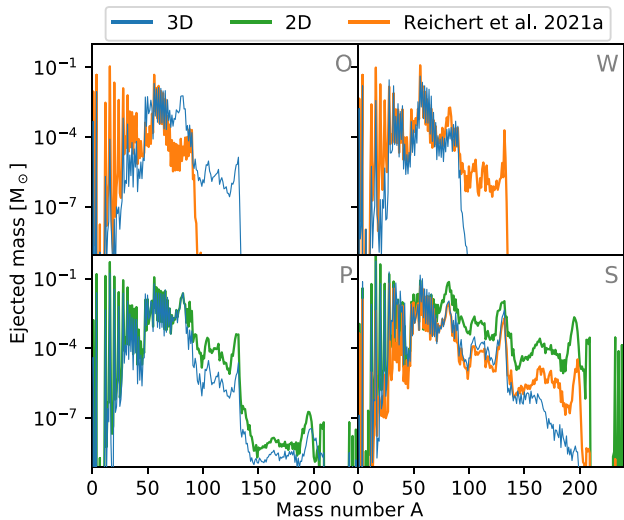


Figure 8. Comparison between the nucleosynthetic yields of 2D axisymmetric and full 3D versions of different models as indicated in each panel. Blue and green lines are models calculated within this work, whereas orange lines refer to 2D models presented in Reichert et al. (2021a). The yields are shown for our lower limit, i.e. the yields obtained by the tracer particles (group 1, Section 2.4).

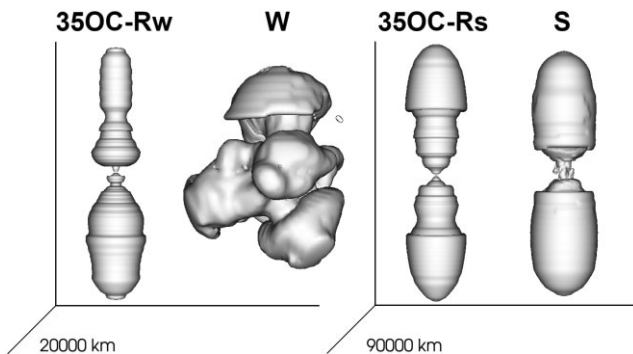


Figure 9. Surface containing the unbound ejecta of models 350C-Rw, 350C-Rs (2D axisymmetric), W, and S (full 3D). The models are shown at 0.46 s, 1.45 s, 1.13 s, and 1.17 s post bounce, respectively. These times were chosen to obtain similar outermost shock positions of 2D and 3D models. The 2D and 3D version of model W develop a different geometry, while the strongly magnetized model S is similar to its 2D counterpart.

Heavier elements ($A > 100$) are exclusively synthesized in the 2D model 350C-Rw (Fig. 8, see also Reichert et al. 2021a), but not the 3D model W. As discussed in Reichert et al. 2021a and AO21, the synthesis of these nuclei is related to a change in the shape of the PNS due to angular momentum transport of the magnetic field at very late times (~ 2 s). The simulation of the 3D model (W) only reached a much earlier time. Although a similar effect cannot be excluded after the end of the simulations, the evolutionary path to it are too specific to deem it very likely.

Similarly to the case of models W and 350C-Rw, the shorter simulation time of model O causes an underproduction of lighter nuclei compared to the axisymmetric version 350C-RO. In 3D, lower neutrino luminosities and shorter ejection time-scales lead to more neutron-rich ejecta containing a component ejected early on that has an electron fraction $Y_e \approx 0.4$ when dropping out of NSE at $T = 7$ GK.

The strongly magnetized models 350C-Rp3 and P evolve fairly similarly to each other. There are slight differences and the 2D model hosts more extreme (low and high) electron fractions. Also this model shows a slightly larger collimation in 2D compared to 3D (Fig. 10). In the southern hemisphere, the 3D model develops a significantly wider beam of proton-rich matter, nearly absent in the 2D model. The combined effects of resolution and enforced axial symmetry drive a more intermittent jet beam in 2D than in 3D. This intermittency results from the strong pinching that the toroidal field drives in axial symmetry. However, the nucleosynthetic fingerprint is qualitatively almost identical. In both models, heavier elements up to the second r-process peak are synthesized by slightly neutron-rich material with $Y_e \sim 0.4$. Both models reach maximum entropies of the order of $\gtrsim 100$ k_B for a small portion of matter ($\sim 10^{-4} M_\odot$).

Among the three versions of the strongest magnetized model, the 3D model S and the 2D model 350C-Rs from Obergaulinger & Aloy (2017); AO21 and OA21 agree well for elements up to the second r-process peak, while abundances of heavier elements are lower in the 3D model. In both models, these elements are located in the jets, whose dynamics does not differ much between 2D and 3D. In particular, we do not observe the development of non-axisymmetric kink instabilities which have the potential to reduce the neutron richness of the jet (Mösta et al. 2014; Kuroda et al. 2020). However, we also observe a slower shock expansion in 3D compared to 2D (Fig. 11, see also Obergaulinger & Aloy 2020). The faster expansion velocity will drive matter faster away from the (anti-)neutrino emitting central PNS. Typical neutrino properties in our simulation are luminosities of $L_{\nu_e} \sim 5 \cdot 10^{52}$ erg s $^{-1}$, $L_{\bar{\nu}_e} \sim 6 \cdot 10^{52}$ erg s $^{-1}$ and mean energies of $E_{\nu_e} \sim 10$ MeV and $E_{\bar{\nu}_e} \sim 13$ MeV. When radiating matter with these neutrino properties until an equilibrium is reached, an electron fraction of $Y_e \sim 0.52$ is obtained (e.g. Qian & Woosley 1996; Arcones & Thielemann 2013; Martin et al. 2018; Miller et al. 2020; Just et al. 2022b). Even though matter will not come into this equilibrium state, it gives an idea that it can be beneficial for neutron-rich conditions to avoid neutrinos. The neutrino flux decrease with the radius squared. Matter that expands fast will therefore be less irradiated by neutrinos than slower expanding matter. This ultimately leads to a slightly lower electron fractions and an r-process in 2D, while the 3D model S is slightly more proton-rich and is therefore not able to host a strong r-process. With a minimum electron fraction of $Y_e \sim 0.23$ (at 7 GK) the 3D model is however at the edge of synthesizing also a larger amount of third r-process peak elements. For this, a minimum of $Y_e \sim 0.20$ would be necessary. There are differences in abundances for $A \gtrsim 70$ between the 2D models 350C-Rs_N and our previous model in Reichert et al. (2021a) because of the longer evolution/simulation time. In model 350C-Rs_N, there is an ejection of very neutron-rich matter at the end of the simulation due to a change of the PNS morphology (see also Fig. 5). This late-time effect did not develop at the final time of our previous model and will be discussed in more detail in the next section (Section 3.3). However, also without this effect, the 2D model shows a much lower electron fraction compared to the respective 3D counterpart (Fig. 10).

Summarizing, we find no universal tendency how the dimensionality impacts the nucleosynthesis. While the 3D version of model O is more neutron-rich and synthesizes heavier elements, model S is less neutron-rich and lacks nuclei of the third r-process peak. We note that 2D models will stay an important tool to trace long-time effects on the nuclear yields (see the case of model 350C-Rw, Reichert et al. 2021a) as 3D models are at the moment still computational too expensive to calculate for the necessary long times.

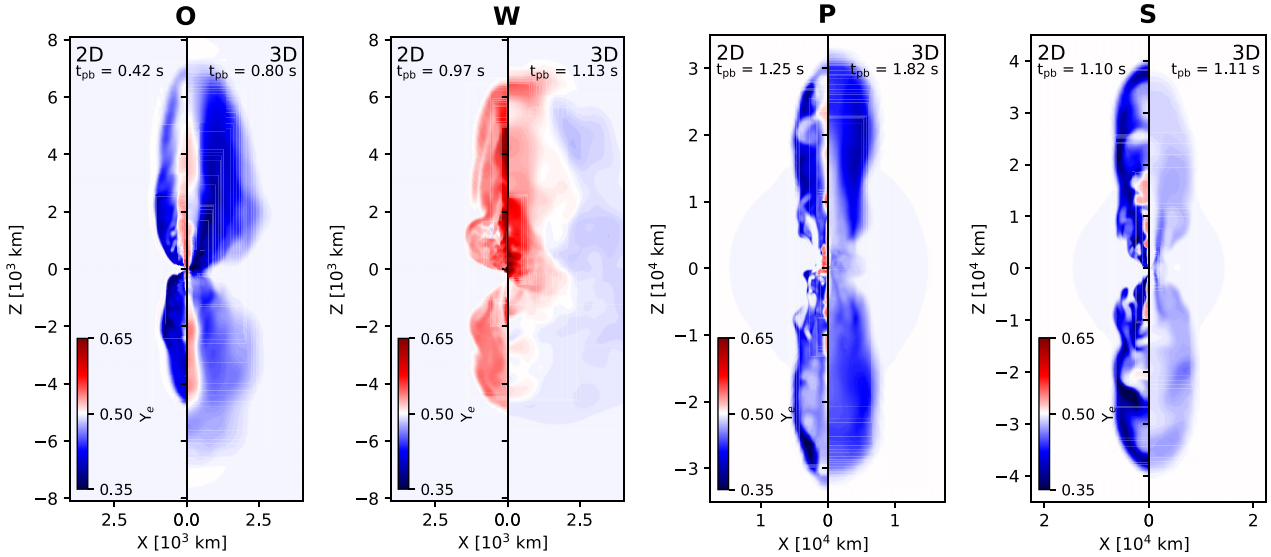


Figure 10. Comparison of the electron fraction between 2D and 3D models. The left-hand panels show a snapshot of the 2D models, the right-hand panels an average of the electron fraction over all ϕ angles in the 3D models. The time of each of the snapshots is selected so that the 2D and 3D versions of the same model reach similar maximum shock radii. We note that an average in the case of the 3D model will blur the minimum and maximum electron fractions.

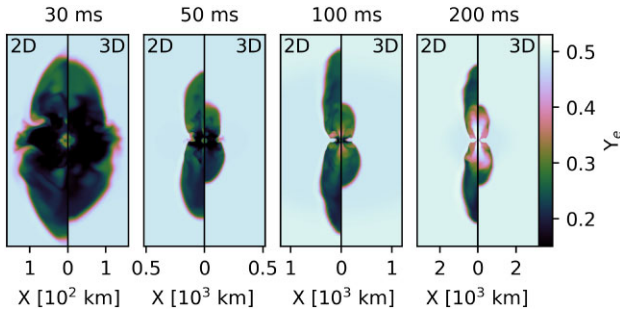


Figure 11. Electron fraction of model 35OC-Rs (left-hand panels) and of a vertical slice of model S (right-hand panels) at different times after bounce. Model 35OC-Rs expands faster and therefore maintains more neutron-rich conditions compared to model S.

3.3 The synthesis of heavy elements

Four of our models (35OC-Rp3, P, 35OC-R_SN, and S) synthesize nuclei with nuclear masses beyond the second r-process peak ($A \gtrsim 130$). All these models have the same stellar evolution pre-supernova star in common, but with a larger poloidal magnetic field strength than in the original 35OC-RO/O models. Hence they all yield powerful magneto-rotational explosions. The r-process occurs in three environments: (i) prompt ejection of matter directly after core-bounce, (ii) late ejection due to changes of the shape of the PNS, and (iii) ejection of high entropy material in the jet (for a brief discussion about proton-rich ejecta see Appendix C). As we describe in the following, the conditions and final abundances (Fig. 12) for the three cases can be very different. Indeed, not all these processes may develop in all models. Specially, process (ii) may be quite stochastic and very much dependent on the evolutionary details of the PNS. Interestingly, the key for mechanism (i) to yield heavy elements is that matter bouncing from the inner stellar core is not halted due to a prompt shock stagnation. This is easier to achieve if a very early magneto-rotational explosion drives a quick supernova shock expansion. If the shock stagnates relatively close to the PNS (where

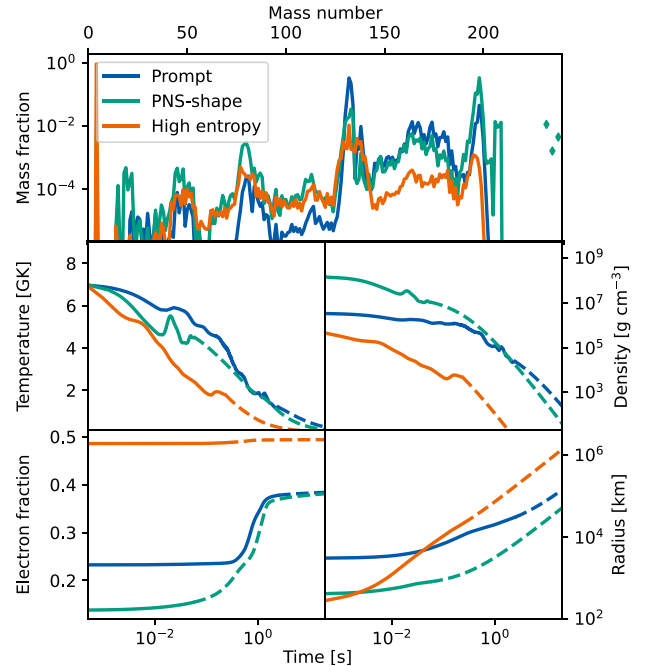


Figure 12. Mass fractions and several hydrodynamic quantities of three representative tracer particles from simulations 35OC-R_SN (prompt and PNS-shape) as well as 35OC-Rp3 (high entropy). The time is relative to the start of the nucleosynthesis calculation at 7 GK, which corresponds to 0 s (prompt), 2.48 s (PNS-shape), and 1.58 s (high entropy) after bounce. All tracer particles host the conditions for a successful r-process. The corresponding neutron-to-seed ratios at 3 GK are 48 (Prompt), 90 (PNS-shape), and 73 (high entropy). Dashed lines indicate extrapolations of the respective quantity, assuming adiabatic (i.e. constant entropy) expansion. The actinides ($A > 220$) are only synthesized within the late ejection that is caused by a reconfiguration of the PNS (cyan diamonds).

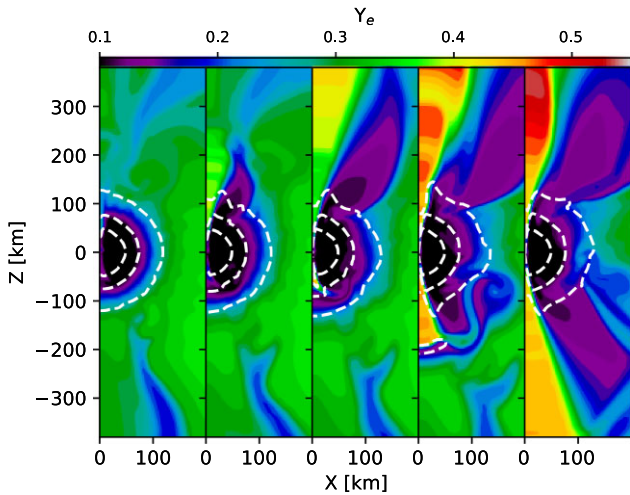


Figure 13. Colour coded is the electron fraction in the centre of model 35OC-Rs_N at four different times (post-bounce). The white, dashed lines are density contours at 10^9 , 10^{10} , and 10^{11} g cm⁻³. The reconfiguration of the PNS shape leads to the ejection of neutron-rich material on short time-scales.

the temperatures still allow for NSE conditions), the intense (anti-)neutrino flux raises Y_e and hampers the production of r-process elements from matter bouncing from the inner stellar core (see below).

A critical factor for a successful r-process is the number of free neutrons available per seed nucleus ($A > 4$), which can capture the neutrons. The corresponding ratio is known as neutron-to-seed ratio defined as

$$r = \frac{Y_n}{\sum_{A>4} Y_A}, \quad (7)$$

where Y_n is the abundance of neutrons and Y_A the abundance of nuclei with mass number A . If matter is ejected promptly after bounce, there is short time for neutrinos to modify Y_e and, thus, it stays very low, e.g. in model 35OC-Rs, we find $Y_e \sim 0.2$ – 0.3 (Reichert et al. 2021a). Once NSE conditions do not hold anymore, the low Y_e leads to a moderate neutron-to-seed ratio of about ~ 50 (at 3 GK). The resulting r-process synthesizes matter up to the third r-process peak. However, we do not find significant production of the heaviest nuclei ($A > 230$), the actinides (Fig. 12, cf. Reichert et al. 2021a).

At later times ($t_{\text{pb}} \gtrsim 2.45$ s), even more neutron-rich matter gets ejected in model 35OC-Rs_N. Its origin is a drastic change in the PNS shape, and it corresponds to the mechanism (ii) mentioned at the beginning of the section. Around $t_{\text{pb}} = 2.5$ s the magnetic pressure and angular-momentum redistribution transform the PNS into a torus like object with an off-centre density maximum (see AO21, and Fig. 13). The new configuration has a lower mass than the PNS. The mass difference of a fraction of a solar mass of neutron-rich gas is ejected within a few milliseconds. We note that this process requires special conditions. Whether it can occur also in 3D remains to be investigated. So far, the 3D counterpart of model 35OC-Rs_N (model S) has not been evolved long enough to corroborate the aforementioned mechanism.

Since the ejection of this matter occurs at the very end of the simulations, our results for the nucleosynthesis may depend to a significant degree on the assumptions made in the extrapolation of the hydrodynamic quantities (dashed lines in Fig. 12, see also Harris et al. 2017), in particular the expansion velocity. We explored the impact on the final yields caused by the choice of velocities

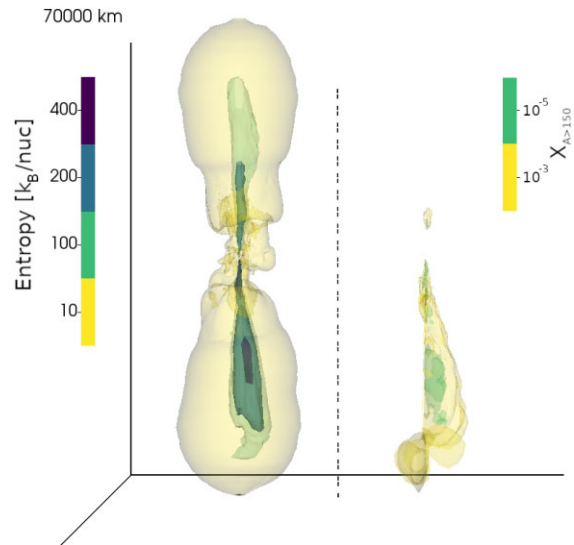


Figure 14. Left: Contours of the entropy per baryon for model P at the end of the simulation ($t_{\text{pb}} = 1.8$ s). Right: Mass fractions of nuclei with $A > 150$. In the right plot, the contours were smoothed with a Gaussian filter for improving the visualization. A clear correlation between heavier synthesized elements and high entropy regions is visible.

and always find a production of elements up to the third r-process peak, with only slight variations of the second to third r-process peak ratio with slightly lower masses of third peak elements for slower expansion velocities. We note that also the neutrino transport (M1) may cause uncertainties in the dynamics of this neutron-rich outflow as it is not able to treat the crossing beams at the rotational axis in an optically thin region (similar to the problems that occur when using M1 in an accretion disc hydrodynamic model; see Chan et al. (2021) for a recent discussion of the limitations of the M1 method in such a situation.) Due to the high neutron-to-seed ratios of ~ 100 , this part of matter even reaches the heaviest synthesized nuclei, the actinides (cyan diamonds in the upper panel of Fig. 12).

Alternatively, high neutron-to-seed ratios can be obtained in less neutron-rich environments when the entropy is sufficiently high (mechanism iii) mentioned at the beginning of the section). In NSE, high entropy material has an excess of nucleons (protons and neutrons) compared to heavier elements. Once the temperature drops during the expansion, NSE conditions eventually break down with a high neutron-to-seed ratio (Meyer 1994; Woosley et al. 1994; Wheeler, Cowan & Hillebrandt 1998; Freiburghaus et al. 1999; Meyer 2002; Thielemann et al. 2017). In the jets of models 35OC-Rp3 and P we find $S \gtrsim 100$ k_B/nuc (Fig. 14). This high entropy leads to large neutron-to-seed ratios of ~ 70 and elements up to the third r-process peak can be synthesized (Fig. 12). The yield is thereby dominated by heavy nuclei ($A \gtrsim 120$) and, in contrast to the other channels of r-process nucleosynthesis, by a high mass fraction of free protons (visible at $A = 1$, upper panel of Fig. 12). We stress that this channel is only able to synthesis heavy elements for slightly neutron-rich conditions. If the electron fraction is $Y_e \geq 0.5$, no heavy elements will be synthesized. The necessary high entropies are not common among our models. They can develop in the inner regions of the jet (the jet beam) when the magnetic structure of the jet is supported by a core of uniform electric current with radius $\tilde{\omega}_m$ (the magnetization radius; Lind et al. 1989; Komissarov 1999; Leismann et al. 2005), and the jet beam is in approximate

Table 3. Yields of radioactive nuclei for different models. The subscript *l* denotes a lower limit as calculated within our models and the subscript *e* denotes our estimate of the final yields as outlined in Section 2.4. The yields are taken at one tenth of the half life of the radioactive nucleus.

Model	$M(^{26}\text{Al})_l$ [$10^{-7} M_\odot$]	$M(^{26}\text{Al})_e$ [$10^{-7} M_\odot$]	$M(^{44}\text{Ti})_l$ [$10^{-5} M_\odot$]	$M(^{44}\text{Ti})_e$ [$10^{-5} M_\odot$]	$M(^{56}\text{Ni})_l$ [$10^{-2} M_\odot$]	$M(^{56}\text{Ni})_e$ [$10^{-2} M_\odot$]	$M(^{60}\text{Fe})_l$ [$10^{-3} M_\odot$]	$M(^{60}\text{Fe})_e$ [$10^{-3} M_\odot$]	$M(^{56}\text{Ni})/M(^{44}\text{Ti})_l$ [$\times 10^3$]
35OC-Rp3	21.0	31.4	20.0	521.7	11.3	97.3	3.1	208.5	0.57
35OC-Rs _N	8.1	–	4.3	–	7.5	–	1.7	–	1.74
P	6.2	15.6	4.2	37.4	3.3	20.8	5.5	11.8	0.79
O	0.4	5.3	0.9	4.9	1.7	10.2	1.2	5.6	1.89
W	0.1	2.5	1.1	4.6	2.2	14.4	0.1	0.1	2.00
S	16.5	16.5	5.9	17.1	10.5	24.8	2.8	8.4	1.78

transverse hydromagnetic equilibrium. Under these conditions, the toroidal magnetic field grows roughly linearly with distance to the rotational axis until $\tilde{\omega} = \tilde{\omega}_m$, and then falls as $1/\tilde{\omega}$, producing strong pinching (see e.g. Leismann et al. 2005). The magnetic pinching yields a high pressure in a region which has lower density than the layer surrounding it, and hence rises significantly the entropy per baryon. The effect is larger when the average beam magnetization grows and the toroidal magnetic field is stronger than the poloidal one. This explains that this channel does not develop in models S, 35OC-Rs, or 35OC-Rs_N, since in these models the poloidal field is close to equipartition with the toroidal field, and the pinching is not as effective. The amount of r-process material ejected via this mechanism is only a small fraction of the total ejecta and adds up to a total of 10^{-8} – $10^{-7} M_\odot$ for models 35OC-Rp3 and P (Fig. 6). While the masses of individual packages of r-process matter ejected by this mechanism may be small, unsteady outflows can create the necessary conditions repeatedly, each episode presumably adding to the total r-process yields. In the case of model P, the total extrapolated value (see Section 2.4) reaches by the end of the simulation up to about a few $10^{-6} M_\odot$.

3.4 Radioactive isotopes

Radioactive isotopes powering to a large degree the electromagnetic emission of SNe play a crucial role in observations related to SN. For example, to classify a SN as HNe one usually uses the explosion energy and the amount of synthesized ^{56}Ni (Nomoto et al. 2006, 2013). In addition to this radioactive isotope, we also investigate the synthesis of ^{44}Ti whose decay is directly observable in young supernova remnants (Grebenev et al. 2012; Seitenzahl, Timmes & Magkotsios 2014). Furthermore, the radioactive elements ^{26}Al and ^{60}Fe can be detected in the interstellar medium (see e.g. Diehl et al. 2021; Diehl 2021, for recent reviews) or in sediments of the ocean crust on Earth (e.g. Wallner et al. 2016; Ludwig et al. 2016). In Table 3, we give the yields of these radioactive elements at the end of the simulation and our estimated extrapolated values according to Section 2.4.

The main contribution of a CC-SN to ^{26}Al originates from hydrostatic burning in the hydrogen layer of the progenitor star before the explosion. For this production channel, the amount of ^{26}Al may reach masses of the order of $10^{-4} M_\odot$ (Karakas 2010; Doherty et al. 2014; Brinkman et al. 2019; Diehl et al. 2021). The data available for our progenitor model (35OC; Woosley & Heger 2006) contain only a reduced set of abundances and does not include information about ^{26}Al (Fig. 4). Therefore, our calculated ^{26}Al yields only reflect the contribution from explosive burning. Until the end of the simulation, none of our models reaches significant ^{26}Al masses compared to what usually is produced during hydrostatic burning. The production of ^{26}Al in explosive environments requires symmetric or proton-

rich conditions with moderate entropy (e.g. Magkotsios, Timmes & Wiescher 2011) that we mainly find in the proton-rich jet (Fig. 15). However, ^{26}Al can also be synthesized during explosive burning with low peak temperatures ($2 \text{ GK} \lesssim T_{\text{peak}} \lesssim 3 \text{ GK}$). The sudden ejection of ^{26}Al at $t_{\text{pb}} \sim 0.9 \text{ s}$ in model S (Fig. 16) is caused by explosive burning in the Oxygen–Neon layer. There, ^{26}Al can be produced via the reaction $^{23}\text{Mg}(\alpha, p)^{26}\text{Al}$ and to smaller extends also via $^{25}\text{Mg}(p, \gamma)^{26}\text{Al}$.

^{60}Fe is thought to originate from neutron captures in the convective envelope during the hydrostatic burning in the progenitor, which is later ejected during the explosion, or in explosive burning inside the He- or C- shell (e.g. Limongi & Chieffi 2006, 2012; Woosley & Heger 2006; Maeder & Meynet 2012; Thielemann et al. 2018; Jones et al. 2019; Lawson et al. 2022). Pre-explosion winds of the AGB stars only play a minor role for the total ejecta mass (Brinkman et al. 2021; Diehl et al. 2021). The total ejected yields of a canonical SN may reach up to $10^{-4} M_\odot$ (Diehl et al. 2021). Similar to ^{26}Al , we only trace ^{60}Fe that is synthesized in explosive conditions via neutron captures. Due to the neutron-rich conditions in our models, they eject a considerable amount of this radioactive element of the order of a few $10^{-3} M_\odot$ (c.f. to $\sim 10^{-5} M_\odot$ or lower in the innermost ejecta of classical CC-SNe Wanajo et al. 2018). Because the synthesized abundances of ^{60}Fe within our simulation are an order of magnitude higher than the ones expected by hydrostatic burning, we conclude that nucleosynthesis during explosive burning dominates the total yields for all of our models except possibly model W. Such high yields offer the potential of detecting ^{60}Fe not only as a diffuse isotope in the ISM, but future telescopes could also detect MR-SNe as point-like sources for a galactic event (Woosley 1997; Diehl et al. 2021). Remarkably, even not extremely magnetized models such as model O synthesize a considerable amount of ^{60}Fe ($\simeq 10^{-3} M_\odot$). Under NSE conditions, the synthesis of ^{60}Fe requires a very specific neutron richness, which is approximately the proton to baryon ratio of the nucleus itself ($Y_e \approx 26/60 \approx 0.43$). Any positive or negative deviation from this ratio leads to a reduction of the ^{60}Fe yields (see also Wanajo et al. 2018; Jones et al. 2019). This is especially visible when comparing the electron fraction of model P (third panel, top row in Fig. 1) with the corresponding ^{60}Fe density (third panel, bottom row in Fig. 15). There are neutron-rich conditions in both hemispheres, north and south. However, in the northern hemisphere there are too many neutrons to synthesize ^{60}Fe and most of the ^{60}Fe is synthesized in the less neutron-rich southern hemisphere. The $^{60}\text{Fe}/^{56}\text{Fe}$ ratio exceeds 10^{-2} for all models except for the more proton-rich model W. This is ~ 6 orders of magnitude higher than the ratio in the early solar system (Trappitsch et al. 2018) or ~ 3 orders of magnitude higher than in the diffusive ISM background, which agrees with the predicted ratio of classical CC-SNe (Diehl 2013; Sukhbold et al. 2016; Austin, West & Heger 2017; Wang et al. 2020; Brinkman et al. 2021).

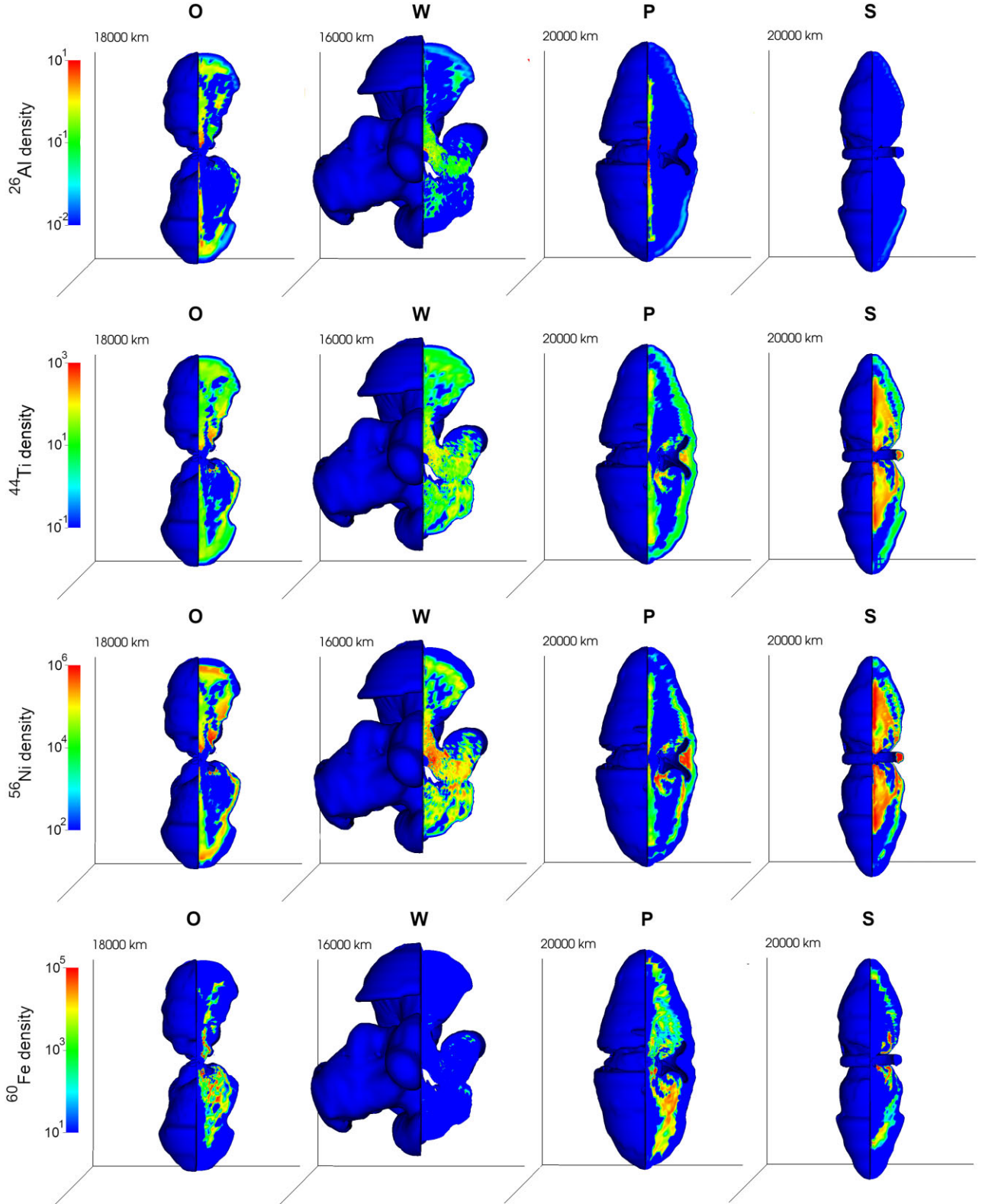


Figure 15. Spatial distribution of the unstable isotopes ^{26}Al (first row), ^{44}Ti (second row), ^{56}Ni (third row), and ^{60}Fe (last row) within unbound matter. The blue surface encloses all unbound matter in each model up to the represented time (i.e. matter unbound up to, approximately the SN shock). The northern and southern octants are cut and a surface perpendicular to the equatorial plane is displayed to visualize the nuclear yields spatial distribution. The mass fraction of these isotopes was taken at one-tenth of their half life, but the position of the tracers was taken at the simulation time $t_{\text{pb}} = 0.80$ s, 1.13 s, 0.63 s, and 0.40 s for models O, W, P, and S, respectively.

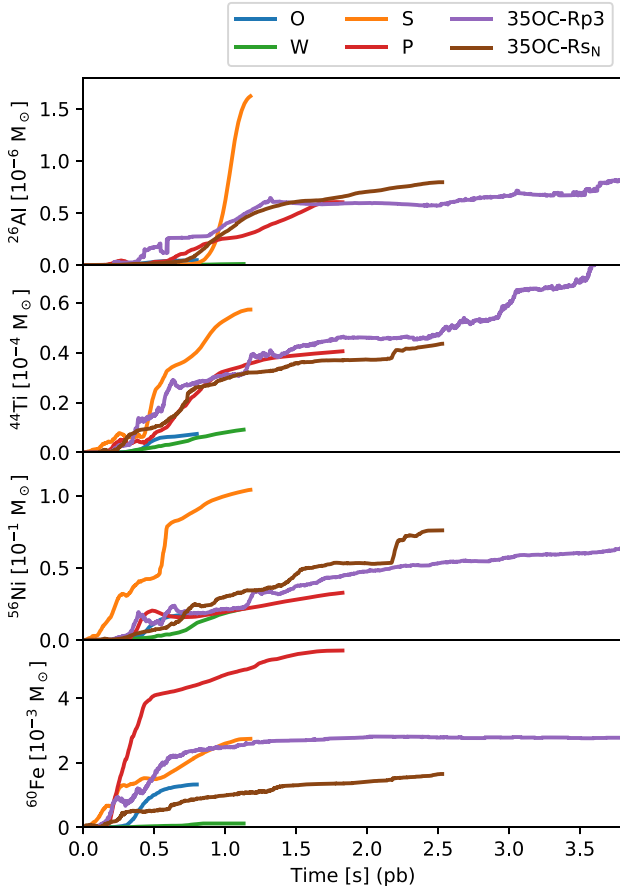


Figure 16. Mass of ejected unstable isotopes ^{26}Al , ^{44}Ti , ^{56}Ni , and ^{60}Fe versus time after bounce. The ejecta mass of all unstable nuclei is still growing.

In our models, we find total ^{44}Ti ejecta between $\sim 10^{-5}$ and $10^{-4} M_{\odot}$ (for our lower limits) and even up to $5 \times 10^{-3} M_{\odot}$ for the extrapolated value of model 35OC-Rp3. The yields are in the range of reported values of SN1987A ($5.5 \times 10^{-5} M_{\odot}$, Seitenzahl et al. 2014) and Cas A ($1.3 \times 10^{-4} M_{\odot}$, Wang & Li 2016). ^{44}Ti is mostly produced in high entropy and symmetric or proton-rich conditions, and it is therefore located in the high entropy jet and at the shock front of the more magnetized models, while it is more uniformly spread within the ejecta of the least magnetized model W (Fig. 15).

Because of its half-life of ~ 6 d and that of its daughter isotope ^{56}Co of ~ 77 d, the decay of ^{56}Ni contributes significantly to the lightcurve of SNe. Huge amounts of ^{56}Ni ($\sim 0.1 - 1 M_{\odot}$ for a $35 M_{\odot}$ ZAMS mass progenitor like ours) may even produce HNe (see Fig. 17 and Nomoto et al. 2006, 2013). Estimated ^{56}Ni masses of SNe associated to long gamma-ray bursts are of comparable magnitude ($0.18 \pm 0.01 M_{\odot}$; Izzo et al. 2019). At the end of the respective simulation, only models 35OC-Rp3, 35OC-RsN, and S reach comparable and large yields of ^{56}Ni , namely $\sim 0.08 - 0.11 M_{\odot}$ (see Table 3). However, nucleosynthesis is still ongoing in all our models. In Table 3 we provide both the yield masses computed until the end of the neutrino-MHD evolution and their extrapolated values according to the methodology of Section 2.4. Noteworthy, for some of the models mentioned above (35OC-Rp3 and S), the extrapolated ^{56}Ni is $\sim 0.25 - 1 M_{\odot}$. Even the weakly magnetized models W and O may produce sufficient ^{56}Ni to be possible HN candidates (Fig. 17) according to our extrapolation method. The

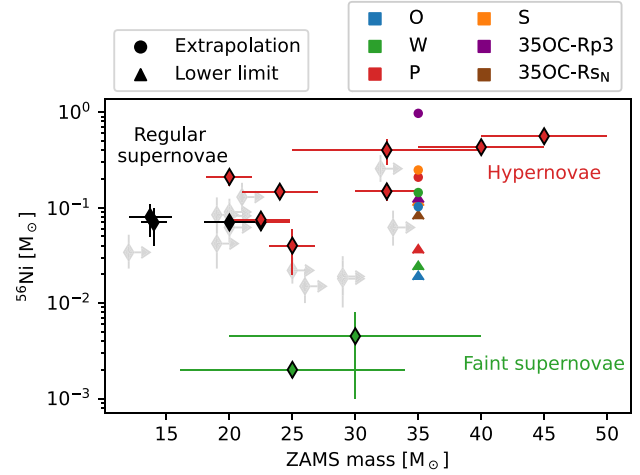


Figure 17. Estimated ^{56}Ni masses of different supernovae versus their ZAMS mass. Hypernovae are indicated as red diamonds, faint supernovae as green diamonds, and regular supernovae as black diamonds. Data is taken from Nomoto et al. (2013). Light grey diamonds shows data by Hamuy (2003). We assumed the ejected mass of the SNe given in Hamuy (2003) as lower limit for the ZAMS mass of the star. The uncertainty of our models is represented by the range between the extrapolated (circles) and the lower limits (triangles). The ejected ^{56}Ni of our models is roughly compatible with observations of HNe. The plot is inspired by Nomoto et al. (2006, 2013).

late-time synthesis of ^{56}Ni may cease, whenever a BH forms, which occurs (or it is expected to happen) in the simulations of AO21 of the 2D counterparts of models O (35OC-RO) and W (35OC-Rw). Whether or not it also happens in 3D requires longer simulation times than we could afford in the present models. In the case of black-hole formation, the final yields would be much closer to the values computed without extrapolating the neutrino-MHD results (see Table 3). The low mass yields are compatible with regular (i.e. no HNe) CC-SNe (e.g. $7 \times 10^{-2} M_{\odot}$ for SN1987A, Seitenzahl et al. 2014 or between $5.8 - 16 \times 10^{-2} M_{\odot}$ for Cas A, Eriksen et al. 2009). However, the ^{56}Ni yields are already too high to be classified as faint SN (Fig 17). The spatial distribution of ^{56}Ni is similar to the one of ^{44}Ti (Fig. 15), i.e. it is located within the jet and at the shock front. The amount of ^{56}Ni that got liberated through the funnel of the jet hereby contributes at maximum to only $\lesssim 15$ per cent of all the created Nickel. Consequently, most of ^{56}Ni is synthesized at the shock front. Therefore, the amount of ^{56}Ni broadly correlates with the explosion energy also in MR-SNe, extending the relation found for ordinary supernovae (e.g. Maeda & Nomoto 2003; Nomoto et al. 2013; Chen et al. 2017; Nomoto 2017; Suwa, Tominaga & Maeda 2019; Grimmett et al. 2021).

The ratio of ^{44}Ti to ^{56}Ni has been proposed as a diagnostic of the entropy in SNe (Nagataki et al. 1997, 1998; Vance et al. 2020; Sato et al. 2021). High entropy environments are characterized by a larger fraction of matter undergoing an α -rich freezeout and, hence, a larger amount of ^{44}Ti is indicative of high entropy conditions. Our models span a wide range of entropy, with the highest values for models 35OC-Rp3 and P. This is directly reflected in their low $M(^{56}\text{Ni})/M(^{44}\text{Ti}) < 10^3$ ratios (see Table 3), while all other models have larger ratios ($\gtrsim 1.7 \times 10^3$).

3.5 The nucleosynthesis of zinc

In addition to their large explosion energy of $\sim 10^{52}$ erg and their high ejected Ni mass of $M(^{56}\text{Ni}) > 0.1 M_{\odot}$ many studies suggest that HNe

may also eject a substantial amount of zinc (e.g. Umeda & Nomoto 2002; Kobayashi et al. 2006; Tominaga et al. 2007; Barbuy et al. 2015; Nishimura et al. 2017; da Silveira et al. 2018; Hirai et al. 2018; Tsujimoto & Nishimura 2018; Ezzeddine et al. 2019; Grimmett et al. 2020, 2021; Yong et al. 2021). Our models have 1/10th of the solar metallicity and thus differ from the interesting case of very metal-poor environments. Nevertheless, the fact that Zn is predominantly produced in hot environments that reach NSE conditions and thus lose memory of the progenitor composition makes our results applicable for the low metallicity case, too. As a consequence, we investigate if our models can explain a high [Zn/Fe] ratio similar to what can be observed in the atmosphere of old stars. The ejected amount of Zn lies between $1 \times 10^{-2} M_{\odot} \lesssim M(\text{Zn}) \lesssim 9 \times 10^{-1} M_{\odot}$. It is mainly synthesized in slightly neutron-rich conditions, and the spatial distribution of Zn is similar to the one of ^{60}Fe (Fig. 15). The nucleosynthetic pathway to Zn differs among our models. While most of them dominantly synthesize the slightly neutron-rich ^{66}Zn , model W synthesizes more ^{64}Zn via the decay of ^{64}Ge due to the less neutron-rich conditions therein. The amount of Fe lies between $1 \times 10^{-1} M_{\odot} \lesssim M(\text{Fe}) \lesssim 1.1 M_{\odot}$ (including the extrapolation as outlined in Section 2.4). Besides Zn and Fe, we also look at the fraction between Zn and first r-process peak elements such as Sr which synthesized about $2 \times 10^{-4} M_{\odot} \lesssim M(\text{Sr}) \lesssim 7 \times 10^{-2} M_{\odot}$. This leads to values of $1.5 \lesssim [\text{Zn}/\text{Fe}] \lesssim 3$ and $-1 \lesssim [\text{Zn}/\text{Sr}] \lesssim 0.5$ (upper rectangles in the left-hand panel of Fig. 18). This exceeds typical values of $[\text{Zn}/\text{Fe}] \sim 0.7$ of observed stars that are proposed to carry signatures of HNe.

However, when comparing the yields of a specific MR-SN to the composition of an individual star, we have to take into account that the ejecta of the explosion did not exclusively form the successor star. Instead they were mixed with the surrounding ISM (see also e.g. Reichert, Hansen & Arcones 2021b), in the process diluting the high yields of elements like Zn or Fe. We therefore estimate the amount of mass the ejecta will mix into. This mixing mass is approximately given by the Sedov–Taylor blast wave solution (e.g. Ryan, Norris & Beers 1996; Magg et al. 2020),

$$M_{\text{gas}} = 1.9 \times 10^4 M_{\odot} E_{51}^{0.96} n_0^{-0.11}, \quad (8)$$

where n_0 is the ambient number density, which we assume to be 1 cm^{-3} . For the explosion energy in units of 10^{51} erg using the diagnostic explosion energy is not adequate, because the latter is still growing by the end of the computed neutrino-MHD evolution. Instead, we assume typical explosion energies in a energy range of observed HNe ($E_{51} = 5\text{--}100$; Nomoto et al. 2006, 2013). These explosion energies lead to mixing masses of $10^5 \lesssim M_{\text{gas}} \lesssim 10^6 M_{\odot}$ (grey region in the right-hand panel of Fig. 18). Assuming a metallicity of $[\text{Fe}/\text{H}] = -1$ and mixing this amount of gas with the ejecta of our models indeed leads to the necessary amounts of [Zn/Fe] to explain the high ratios of some stars (lower coloured regions in the left-hand panel of Fig. 18, the dashed lines correspond to ratios for lower mixing masses). We note that a high [Zn/Fe] is obtained in all of our models and not only in the most energetic model explosions. Even in the least magnetized models that are closer in terms of explosion energy to regular CC-SNe we obtain an excess in Zn (also compare to similar possible high fractions in other regular multidimensional CC-SNe models Eichler et al. 2018; Wanajo et al. 2018; Sieverding et al. 2020; Sandoval et al. 2021). The fact that the [Zn/Fe] ratio is low for HNe in 1D models may be the result of missing physics such as downflows (cf. also to Grimmett et al. 2018, who were unable to reproduce large [Zn/Fe] within 1D HNe models). Nevertheless, when including mixing, our models can also

explain [Zn/Fe] ratios up to ~ 1.5 dex in agreement with the typical values suggested for HNe.

3.6 Candidates for superluminous supernovae?

MR-SNe have also been suggested as explanations for SLSNe (e.g. Quimby et al. 2011; Gal-Yam 2012; Inserra et al. 2013b; Soker & Gilkis 2017; Gal-Yam 2019; Nicholl 2021; Soker 2022). This is because MR-SNe bring the promise of producing larger amounts of ^{56}Ni than ordinary CCSNe, and they may also host protomagnetars, which may act as central engines releasing energy in the ejecta that decisively contribute to the overall luminosity of the explosion.

We apply an extended version of the simplified model for supernova light curves of Dado & Dar (2015) to the results of our simulations. It is based on the assumption of a spherical cloud of hot gas dominated by photon pressure and expanding with a given velocity into the surrounding medium. The thermal energy of the gas changes due to adiabatic expansion, the emission of photons diffusing out of the cloud, and radioactive heating. For the latter effect, while the original prescription only accounted for the decay chain $^{56}\text{Ni} \rightarrow ^{56}\text{Co} \rightarrow ^{56}\text{Fe}$, we include a larger set of isotopes with abundances obtained by our detailed nucleosynthesis calculations.

We assume that photons diffuse out of the cloud on a time-scale $t_{\text{diff}} \approx t_r^2/t$ with t_r being dominated by Compton scattering,

$$t_r \approx \sqrt{\frac{3M_{\text{ej}} f_e \sigma_T}{8\pi m_p c V_{\text{ej}}}}. \quad (9)$$

Here, M_{ej} is the total ejected mass, f_e the fraction of free electrons (~ 0.3 ; see Dado & Dar 2015), $\sigma_T \approx 6.5 \times 10^{-25} \text{ cm}^2$ the Thomson cross section, c the speed of light, and V_{ej} the ejecta velocity. We estimate the velocity of the models by assuming that the total explosion energy and ejecta mass, obtained from the final state of the neutrino-MHD simulations, will be converted into kinetic energy, i.e.

$$V_{\text{ej}} = \sqrt{2 \frac{E_{\text{ej}}}{M_{\text{ej}}}}, \quad (10)$$

which leads to velocities of the order of a few 10^4 km s^{-1} . The bolometric luminosity is given by (equation 4 in Dado & Dar 2015)

$$L = \frac{e^{-t^2/2t_r^2}}{t_r^2} \int_0^t t e^{-t^2/2t_r^2} \dot{E} dt. \quad (11)$$

The heating rate \dot{E} is computed as sum over all nuclear decay channels (here for an individual nucleus N) according to

$$\dot{E}(N) = \left(\sum_i \lambda_i Y_N Q_i \right) \times M \quad (12)$$

with the decay constant λ_i , the corresponding Q-value of the reaction Q_i and the abundance of the parent nucleus Y_N . The energy released in the decays is split into (i) photons, \dot{E}_{γ} , (ii) positrons or electrons, $\dot{E}_{e^{\pm}}$, (iii) α -particles, \dot{E}_{α} , and (iv) neutrinos, $\dot{E}_{\nu_e, \bar{\nu}_e}$. Additionally, we assume that the energy released in electron captures escapes entirely via neutrinos. We have $\dot{E}_{\text{tot}}(N) = \dot{E}_{\gamma} + \dot{E}_{e^{\pm}} + \dot{E}_{\alpha} + \dot{E}_{\nu_e, \bar{\nu}_e}$ for each nucleus N . We take into account that a part of the photons leaves without depositing energy in the gas and estimate the fraction of photons that thermalize in the ejecta (equation 7 in Dado & Dar 2015),

$$A_{\gamma} \approx 1 - e^{-\tau_{\gamma}}. \quad (13)$$

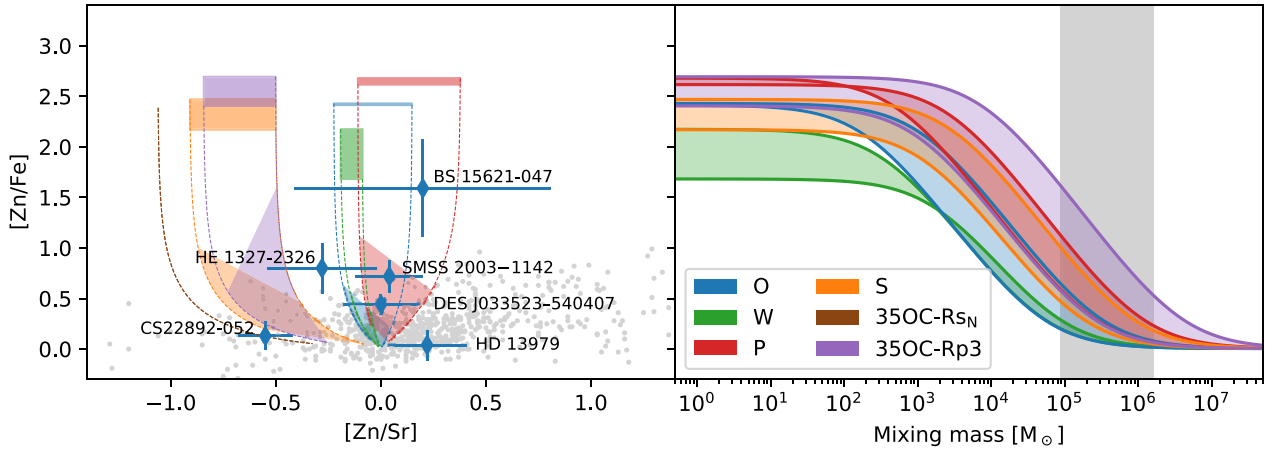


Figure 18. The left-hand panel shows $[Zn/Fe]$ versus $[Zn/Sr]$. Every grey dot is a star taken from Westin et al. (2000), Hill et al. (2002), Aoki et al. (2002), Cowan et al. (2002), Ivans et al. (2003), Christlieb et al. (2004), Barbuy et al. (2005), Aoki et al. (2005), Barklem et al. (2005), Sivarani et al. (2006), Cohen et al. (2006), Masseron et al. (2006), Honda et al. (2007), Aoki et al. (2007), Aoki et al. (2008), Lai et al. (2008), Cohen & Huang (2009), Bonifacio et al. (2009), Mashonkina et al. (2010), Frebel et al. (2010), Roederer et al. (2010), Cohen & Huang (2010), Honda et al. (2011), Hollek et al. (2011), Allen et al. (2012), Kirby & Cohen (2012), Cui, Sivarani & Christlieb (2013), Cohen et al. (2013), Gilmore et al. (2013), Ishigaki, Aoki & Chiba (2013), Frebel, Simon & Kirby (2014), Roederer et al. (2014), Placco et al. (2015), Hansen et al. (2015), Jacobson et al. (2015), Li et al. (2015), Siqueira-Mello et al. (2015), Skúladóttir et al. (2015), Placco et al. (2016), Kirby et al. (2017), Mishenina et al. (2017), Roriz et al. (2017), Hansen et al. (2017), Holmbeck et al. (2018), Sakari et al. (2018), Bandyopadhyay et al. (2018), Ji & Frebel (2018), Gull et al. (2018), Cain et al. (2018), Mardini et al. (2019), Purandardas et al. (2019), and Ji et al. (2019), accessed via the SAGA database (Suda et al. 2017). Additionally, we added stars from Reichert et al. (2020). Blue diamonds are chosen r-process enhanced stars namely He 1327-2326 (Ezzeddine et al. 2019), BS 15621-047 (Allen et al. 2012), SMSS 2003-1142 (Yong et al. 2021), DES J033523-540407 (Ji & Frebel 2018), HD 13979 (Roederer et al. 2014), and CS22892-052 (Snedden, Cowan & Lawler 2003). Coloured boxes show the range of ratios for the individual MR-SNe models using the lower and estimated ejected yields into account (see Section 2.4). Dashed lines indicate the ratio when solar scaled material gets mixed into the ejecta. Here, solar scaled material is material of originally solar abundances in which we reduce all abundances but hydrogen by the same factor and add the excluded mass to hydrogen to conserve the total mass until we reach $[Fe/H] = -1$. The coloured shapes indicate the range of ratios when mixing $\sim 10^5 - 10^6 M_\odot$ of solar scaled gas into the ejecta. The right-hand panel illustrates $[Zn/Fe]$ ratios in dependence of different mixing masses. The grey region shows the expected mixing masses that we obtain for assumed explosion energies between 10^{52} and 10^{53} erg. Our models are able to explain stars with an excess of $[Zn/Fe]$.

Here, τ_γ is the optical depth given by

$$\tau_\gamma = \frac{3M_{ej}\sigma_t}{8\pi m_p V_{ej} t^2}. \quad (14)$$

The so called Klein-Nishina energy transfer cross-section σ_t is dependent on the average photon energy \bar{E}_γ of the decay³ and calculated via (e.g. Attix 2004)

$$\begin{aligned} \sigma_t(\bar{E}_\gamma) = 2\pi r_e^2 & \left[\frac{2 \times (1+x)^2}{x^2 \times (1+2x)} - \frac{1+3x}{(1+2x)^2} \right. \\ & - \frac{(1+x) \times (2x^2 - 2x - 1)}{x^2 \times (1+2x)^2} - \frac{4x^2}{3(1+2x)^3} \\ & \left. - \left(\frac{1+x}{x^3} - \frac{1}{2x} + \frac{1}{2x^3} \right) \times \ln(1+2x) \right] \quad (15) \end{aligned}$$

with the electron radius r_e and the photon energy in units of the electron rest energy $x = \bar{E}_\gamma/m_e c^2$, where m_e is the electron mass. Because σ_t and the fractions of energy released as photons (f_γ), positrons/electrons (f_{e^\pm}) and α -particles (f_α) differ between decay reactions, we obtain the contributing energy as sum over all decaying nuclei,

$$\dot{E} = \sum_N (A_\gamma(N)f_\gamma(N) + f_{e^\pm}(N) + f_\alpha(N)) \times \dot{E}_{tot}(N). \quad (16)$$

³From ENSDF database as of 1/12/21. Version available at <http://www.nndc.bnl.gov/ensarchivals/>

We neglect the impact of neutrinos on the supernova light curve and assume that they are radiated away without any further interaction. Trivially, $f_\gamma + f_{e^\pm} + f_\alpha + f_{\nu_e, \bar{\nu}_e} = 1$ holds. In equation (16) we also neglect energy from pair annihilation.

For early times (~ 1 d), most of the energy released by decays thermalizes, heats the gas, and thus contributes to the light curve. The light curve is dominated by the radioactive decay of ^{56}Ni initially and of ^{56}Co later on. However, the decay of other nuclei also slightly contributes to the light curve, increasing the peak luminosities by 38 per cent, 13 per cent, 37 per cent, 13 per cent, 13 per cent, and 24 per cent for models O, W, P, S, 35OC-Rp3, and 35OC-Rs_N, respectively.

The luminosity of all models is increased by at least 13 per cent in comparison to a model that considers the decay chain of ^{56}Ni only. An additional boost up to a 38 per cent higher peak luminosity can come from the decay chain $^{66}\text{Ni} \rightarrow ^{66}\text{Cu} \rightarrow ^{66}\text{Zn}$. This decay chain contributes predominantly to heating of the gas via the decay of the short-lived ^{66}Cu (due to the nuclear properties, see Table 4, c.f. to the nuclear properties given in Nadyozhin 1994; Wu et al. 2019; Shingles et al. 2020), powered by the longer lived ^{66}Ni . For the synthesis of ^{66}Ni the neutron-richness plays a dominant role. We find a major contribution to the light curve if more matter drops out of NSE ($T = 7$ GK) with $0.42 < Y_e < 0.47$ than with $Y_e > 0.47$, which is the case for models O, P, and 35OC-Rs_N.

At times $100 \lesssim t \lesssim 1000$ d the light curve is dominated by the decay of ^{56}Co emitting positrons that subsequently thermalize (Seitenzahl, Taubenberger & Sim 2009; Dado & Dar 2015). For even later times,

Table 4. β -decay properties of selected nuclei. The table contains the name of the parent nucleus, half-lives (note that $\lambda = \ln 2/T_{1/2}$), released energies, fraction of released energy in form of photons, average photon energy per decay, fraction of energy in form of electrons or positrons, and the fraction of energy in form of neutrinos. Half-lives and Q-values are taken from the JINA Reaclib database (Cyburt et al. 2010), while all other properties are taken from the ENSDF database (Brown et al. 2018).

Parent	$T_{1/2}$ [d]	Q [MeV]	f_γ	\bar{E}_γ [MeV]	f_{e^\pm}	$f_{\nu_e, \bar{\nu}_e}$
^{56}Co	77.2	4.57	0.787	1.13	0.028	0.185
^{57}Co	272.0	0.84	0.154	0.07	0.017	0.829
^{56}Ni	6.1	2.13	0.798	0.48	0.004	0.198
^{57}Ni	1.5	3.26	0.595	0.86	0.049	0.356
^{66}Ni	2.3	0.25	0.000	–	0.291	0.709
^{66}Cu	0.004	2.64	0.037	1.03	0.404	0.559
^{72}Ga	0.6	4.00	0.692	1.21	0.118	0.190

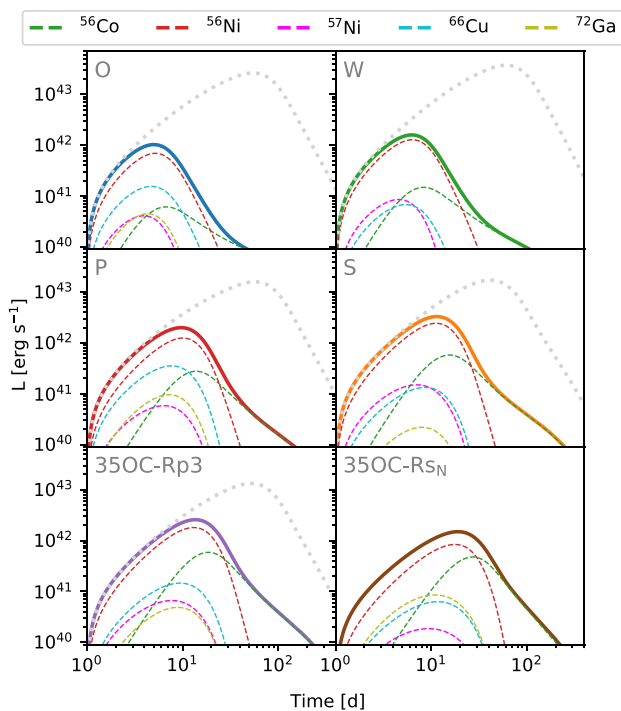


Figure 19. Light curve as estimated with ejected masses and yields at the end of the simulation (coloured solid lines). Coloured dashed lines show the individual light curves due to the radioactivity of the most contributing nuclei. The light-grey dotted line indicates the light curve using the extrapolated values of ejected matter described in Section 2.4.

the assumptions of our simple model may break down as the ejecta become optically thin.

The peak luminosities lie within $10^{42} - 4 \times 10^{42} \text{ erg s}^{-1}$ (Fig. 19) in a range which is expected for moderate luminous supernovae (Inserra et al. 2013a). Superluminous supernovae usually exceed $10^{43} \text{ erg s}^{-1}$ (see e.g. Gal-Yam 2019, for a recent review). Indeed, when using the extrapolated value of the ejected mass and nickel masses outlined in Section 2.4, we obtain peak luminosities exceeding $10^{43} \text{ erg s}^{-1}$ (grey dashed lines in Fig. 19).

However, so far we only investigated a simplified light curve model that assumes spherical symmetry. The impact of a viewing angle dependence of non-spherical models on the luminosity depends on the shape and ^{56}Ni distribution. The variation may lie between \sim

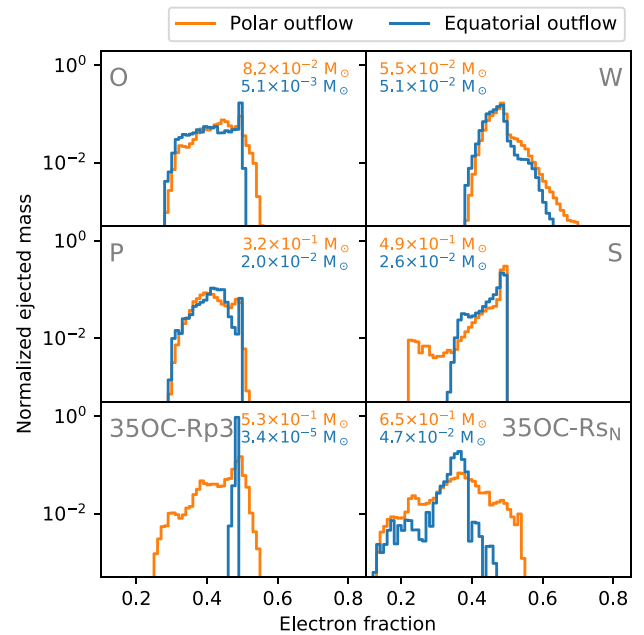


Figure 20. Histograms of the electron fraction at $T = 7 \text{ GK}$ normalized to the ejected mass in the equatorial and polar region, respectively. The outflow is divided into a polar one (orange) defined as $0 \leq \theta \leq 60$ and $120 \leq \theta \leq 180$ as well as an equatorial one (blue) defined as $60 < \theta < 120$. The histogram is extracted at the end of the simulations (Table 1). The coloured text indicates the total ejected mass in each of the components. We note that only ejecta with $T \geq 7 \text{ GK}$ is considered here.

10 – 40 per cent, having a higher luminosity at the equator compared to the poles (Wollaeger et al. 2017; Barnes et al. 2018). Furthermore, we observe a certain structure in the distribution of ^{56}Ni (Fig. 15), while our light-curve model assumes that all radioactive sources are located in the centre. In model S, most of the ^{56}Ni is even behind a fairly opaque lanthanide enriched shell (see the shell of low electron fraction in Fig. 1). The structure possesses some analogy to the ‘lanthanide curtain’ found in models of neutron star mergers (NSM) by, e.g. Perego et al. (2014). This in-homogeneity will introduce further variations in the light-curve. A better mixing can shift the peak of the light-curve to an earlier time (Taddia et al. 2016, 2019).

Additionally, we note that the light-curve model does not include any luminosity enhancing effects that could arise from an interaction with the circumstellar matter and that could be significant. It has been pointed out previously that these interactions could be responsible for the occurrence of SL-SNe (e.g. Jerkstrand et al. 2020, and references therein).

We note that there could also be an interesting dependence of the colours of the light-curve due to the quite different conditions involved when looking at ejecta at the equator and at the polar region (see Fig. 20). The distribution of the electron fraction differs in the ejecta along the polar and along the equatorial regions due to the slower expansion of the latter ejecta, which allows for a more efficient neutrino heating in the equatorial plane. Even though the ejected mass in the equatorial region is rather small in all jet-driven models, we observe differences in the different directions. Model W is an exception. This model is close to what one would expect in a regular CC-SNe and explodes rather spherical and the explosion is not driven by jets (see Appendix C). The distribution of the electron fraction is therefore more similar in the equatorial and jet direction. The distinct distributions of the electron fraction may yield the key to distinguish usual CC-SNe and jet-driven MR-SNe in the future.

Summarized, the models here may reach the necessary peak luminosities to be classified as SLSNe even only accounting for the radioactive contribution to the light curve (i.e. not even including the potential contribution of the central engine as in OA22). However, the general shape of the light curve is dominated by the decay chain of ^{56}Ni . As pointed out by several authors (e.g. Inserra et al. 2013b; Gal-Yam 2019) the slope of the decaying light curve of observed SLSNe is often incompatible with a slope that is inferred by the decay of ^{56}Ni and ^{56}Co . For these cases, the accretion on a central BH or the spin-down of a magnetar in the centre of the SLSN has been proposed as energy source of the extremely high luminosities (Kasen & Bildsten 2010; Woosley 2010; Dessart et al. 2012; Inserra et al. 2013b; Chatzopoulos et al. 2013; Mazzali et al. 2014; Nicholl et al. 2014, 2015; Metzger et al. 2015; Obergaulinger & Aloy 2022). Nicholl, Guillochon & Berger (2017) and De Cia et al. (2018) find typical required magnetic field strengths of $B \sim 10^{14}$ G and spin periods of $P \sim 2$ ms of the magnetar to match light curves of SLSNe. For those of our models that avoid BH formation, i.e. most likely models O, P, S, 35OC-Rp3, and 35OC-Rs_N, the PNS does indeed fulfil these conditions. The investigation of the impact of a central engine is beyond the scope of this work, but we refer the reader to the simplified light curve models obtained in OA22. In these models, the central engine contribution is dominant, and allows for the possibility of extremely bright events. The obtained radioactive peak luminosities here are higher than the ones for the models presented in OA22, because of the various additional radioactive energy sources (there only Ni and Co were considered) and, specially, because of the extrapolation of the radioactive yields following the methodology of Section 2.4.

4 DISCUSSION AND CONCLUSIONS

We presented the detailed nucleosynthesis of long-time 2D models as well as 3D models of MR-SNe evolved to final times of the order of at least 1 s for the 3D models and up to 9 s for one 2D model. For some of the new 3D models, axisymmetric versions were presented in our previous article Reichert et al. (2021a). The simulations were performed with a sophisticated energy-dependent M1 neutrino transport (Just et al. 2015), which allows for a reliable determination of nucleosynthesis-relevant properties such as the electron fraction of the ejecta. The set of models includes one case of an explosion driven mostly by neutrino heating and several magnetorotational explosions with polar jets.

All the models in this study, regardless of their dimensionality (2D or 3D), are variations of a single magnetized, fast-rotating, massive stellar progenitor. These variations are broadly compatible with the uncertainties carried by 1D stellar evolution models. Here, we have extended our previous results (Reichert et al. 2021a) to 3D models and to longer 2D evolutionary times. That has allowed us to show that not only the dynamics (Obergaulinger & Aloy 2017, OA21), the explosion mechanism (Bugli et al. 2020; Obergaulinger & Aloy 2020), and the compact remnant type (AO21) are critically dependent on (order of magnitude) variations of the rotational rate and magnetic field strength, but also the nucleosynthetic yields depend significantly on these initial conditions.

We computed the detailed nucleosynthesis by applying the large nuclear network WINNET with 6545 isotopes to Lagrangian tracer particles following the dynamics of the ejecta. For this purpose, we sampled the unbound material at the final time of the simulations with tracers, and evolved them backward in time according to the velocity field of the neutrino-MHD models. To accurately sample the ejecta, of the order of a solar mass, the tracers have different masses

with an upper limit of $10^{-4} M_{\odot}$, leading to a total number of tracers of $\mathcal{O}(10^4) - \mathcal{O}(10^6)$. We reduce the computational effort by binning the tracers into groups with similar physical properties.

Despite the long simulation times, the ejection of mass has not been finished when the models were terminated. We developed a method to estimate the final ejected mass fractions. For this, we use an extrapolation procedure to approximately determine the conditions relevant for nucleosynthesis. While the uncertainties of this method are considerable, it allows us to obtain estimates of the yields of several elements that would otherwise be underestimated.

We compared the nucleosynthetic results of the 3D models with their respective 2D versions. The dynamics (see OA21), but also the calculated yields can differ significantly. Consistently, there is no universal trend in neutron-richness between 2D and 3D. On the one hand, the nucleosynthetic imprints of long time effects that are visible in the long simulated 2D models cannot be investigated in their 3D version due to the shorter simulation times. On the other hand, the different dynamics of the 3D models can leave a fingerprint in the nucleosynthetic yields. Therefore both, 2D and 3D models, will stay important tools for the investigation of MR-SNe in the future.

We find three major mechanisms to synthesize r-process elements. The first one is connected with an early and fast ejection of neutron-rich matter. This matter will later be located in a cocoon around the jet as reported already in earlier studies (Winteler et al. 2012; Nishimura et al. 2015, 2017; Mösta et al. 2018; Reichert et al. 2021a). This production mechanism may be less favorable in 3D given the less neutron-rich conditions of model S (OA22). However, model S is nevertheless very neutron-rich with minimum electron fractions of $Y_{e, \text{min}} \sim 0.23$ (at $T = 7$ GK) which is only slightly larger than the boundary of 0.20 that have been found to be sufficient for the production of third r-process peak elements. Given this marginal difference, a slight change in the setup (either numerical or physical) may enable a full r-process by this mechanism also in 3D. The long simulation times enabled us to investigate a second mechanism. If the magnetic field is strong enough, it can have a strong impact on the shape of the PNS. In model 35OC-Rs_N this even led to a transition of the PNS to a toroidal configuration in the centre. This process ejects very neutron rich material from the PNS itself on short time-scales (see also AO21), which ultimately lead to an r-process synthesizing heavy elements that include the actinides. This ejection mechanism is not unique among our models as we found a similar behaviour already in model 35OC-Rw presented in Reichert et al. (2021a). However, it has to be shown that this effect can also occur in full 3D simulations and over a broader set of initial models (including different masses, and mechanisms for angular momentum transport). Determining the conditions in the massive collapsing star that yield to the actinide production is highly uncertain with only a few models. But the model in which this distinctive feature has happened harbours a strong ($\sim 10^{12}$ G), large-scale, poloidal magnetic field in equipartition with the toroidal magnetic field. Although this field is not directly obtained from a consistent stellar evolution, the uncertainties still remaining in the secular (1D) modelling of massive stars, would likely allow for the realization of a quantitatively similar case (see AO21, for a more detailed discussion, and Griffiths et al. (2022) for the potential action of MRI in the topology of the magnetic field). The last mechanism is driven by high entropies rather than very neutron-rich conditions. Two of our models, 35OC-Rp3 and P, showed high entropies (exceeding $S > 200 k_{\text{B}}$) in the beam of the magnetically driven jets. Under these conditions the neutron-to-seed ratio can exceed >70 and is therefore high enough to perform a full r-process (e.g. Woosley et al. 1994; Wheeler et al. 1998; Freiburghaus et al. 1999; Meyer 2002; Thielemann et al. 2017).

Thus, summarizing the r-process results, we find two aspects within our 3D models: (i) The strongest pre-collapse magnetic fields lead to the strongest r-process ejecta in a cocoon around the jet, resulting in an early and fast ejection (consistent with earlier investigations). Whether such strong pre-collapse magnetic fields result from realistic stellar evolution calculations has to be verified in the future. (ii) While the hope that an r-process can occur for very moderate Y_e -values, resulting from earlier neutrino interactions with matter during the explosion phase, has been raised (e.g. by Takahashi, Witt & Janka 1994; Woosley et al. 1994), if high entropies are obtained, later CCSN simulations never supported such conditions. In the present paper we have found such conditions in some models during the later phase of the explosion. Should these conditions be recreated in nature, they would be a fingerprint of the existence of a collimated/jetted ejecta inside the star, since they require magnetized jet beams where the toroidal magnetic field is larger than the poloidal one, thus allowing for a strong beam pinching. However, the resulting nucleosynthetic pattern is probably not one of a full solar-type r-process.

Even though we have shown that MR-SNe are able to host a small portion of matter undergoing an r-process also in 3D, there are some caveats when considering MR-SNe as dominant astrophysical production sites of the r-process. If we consider a typical mixing mass of $10^5 M_\odot$ and assume that the ejecta is homogeneously mixed into pure hydrogen we also obtain a minimum metallicity of the remnant composition. Taking the considerable amount of iron given for our extrapolated final yields, this would lead to remnant metallicities with $[\text{Fe}/\text{H}] \gtrsim -2.5$ for the possible r-process candidate models S and P. However, newly born stars will not form from the remnant composition, but might rather have only a 10 or 1 per cent admixture from a nearby event. Therefore, extending the mixing mass to quite extreme $10^6 M_\odot$ would also extend the limit to $[\text{Fe}/\text{H}] \gtrsim -3.5$, which becomes consistent with low-metallicity observations. A (very extreme) explosion energy of 10^{53} erg would already lead to such a low metallicity in the remnant. Similar arguments can be applied for Collapsars. For these events, model O and W are possible candidates. If a collapsar (or BH) forms, our iron amount will be closer to our lower limit, i.e. as obtained by our tracer particles. A further iron contribution that we here do not account for will come from ejecta of the later forming accretion disc. For model O and W, a likely maximum mixing mass of $10^5 M_\odot$ result in $[\text{Fe}/\text{H}] \approx -3.5$ as lower metallicity limit, indicating similar conditions for describing very metal-poor r-process enhanced stars with collapsars. Therefore, MR-SNe and collapsars may occur early in galactic history, earlier than merging neutron stars, permitting with their iron ejecta to describe very metal-poor r-process enhanced stars down to $[\text{Fe}/\text{H}] \approx -3.5$. Additionally, we notice that our extrapolations of iron also limit the ratio $[\text{Eu}/\text{Fe}]$. While the strongest magnetized 3D model S reaches values of $[\text{Eu}/\text{Fe}] \approx 1.5$ that fit with very r-process enhanced stars (r-II stars, $[\text{Eu}/\text{Fe}] > 1$, Beers & Christlieb 2005), model P only reaches $[\text{Eu}/\text{Fe}] \approx 0.7$ and a successor star would therefore be at most categorized as less enriched r-I star ($0.3 < [\text{Eu}/\text{Fe}] < 1$; Beers & Christlieb 2005). We stress that these are upper limits that are unlikely obtained as frequently occurring CC-SNe could further contribute to iron, but not to europium thus lowering $[\text{Eu}/\text{Fe}]$. Whether these values are sufficient to describe the evolution of europium in the early Universe has to be addressed by more complex galactic chemical evolution models (e.g. Schönrich & Weinberg 2019; Kobayashi, Karakas & Lugaro 2020; van de Voort et al. 2020; Cavallo, Cescutti & Matteucci 2021; van de Voort et al. 2022), combined with progenitors with lower metallicity, and/or longer simulations in the future.

Additionally, it seems to be challenging to synthesize a considerable amount of actinides within our 3D models except via high entropy conditions. Model P could reach $[\text{Th}/\text{Eu}] \approx 0.37$ (after 1 Gyr); however, this value is based on our extrapolation and involves therefore large uncertainties. On the other hand, model S reaches $[\text{Th}/\text{Eu}] \approx -3.9$ only. This value might be less uncertain as we expect that the ratio is not modified significantly with ongoing simulation time. This is a difference compared to a confirmed r-process site, NSM, which are expected to robustly eject larger amounts of actinides (see e.g. Horowitz et al. 2019; Cowan et al. 2021; Wu & Banerjee 2022, for recent reviews). Judging from our models, stars with a high amount of actinides (as, e.g. reported in Yong et al. 2021) are extremely challenging to describe with a dominant contribution of MR-SNe. On the other hand, a certain variability in the actinides has been observed in form of so called ‘actinide boost’ stars (Roederer et al. 2009; Mashonkina, Christlieb & Eriksson 2014; Holmbeck et al. 2018, 2019; Eichler et al. 2019; Farouqi et al. 2021). While the existence of actinide boost stars may be explained with different contributions of the NSM disc and dynamical ejecta only (Eichler et al. 2019; Holmbeck et al. 2019) an additional contributing source can not be excluded. This is furthermore underlined by the observation of an ‘actinide deficient’ star (Ji & Frebel 2018) which could possibly be explained by our model S. For this group of stars, there is only one representative observed so far and it is therefore a very rare class of stars. As a consequence, MR-SNe may only give a small contribution to the total r-process content in our Universe. On the other hand, the sparsity of these stars can also be an observational bias as deficiencies are harder to detect than elemental enhancements, especially for the actinides that are challenging to detect. We can, however, not fully neglect a later (after the simulation ended) contribution to the actinides by the outflow of a possibly forming collapsar. Whether these outflows are able to contribute to the synthesis of actinides is still a matter of ongoing investigations (Siegel et al. 2019; Miller et al. 2020; Just et al. 2022a) and goes beyond the scope of this work.

We studied the viability of MR-SNe as candidates for HNe or SLSNe. Two of our models, model 35OC-Rs_N and S, reach explosion energies that are compatible with those of observed HNe (Nomoto et al. 2013). We therefore investigated the amount of unstable nuclei such as ^{26}Al , ^{44}Ti , ^{56}Ni , and ^{60}Fe that are also observed in HNe. The ejected amount of ^{44}Ti lies with $10^{-5} - 10^{-4} M_\odot$ in the range of regular CC-SNe. While only two models reach ^{56}Ni masses of $> 0.1 M_\odot$ necessary for HNe (Nomoto et al. 2013), the extrapolated values of all other models indicate that such masses are also possible if the simulations were carried out for a longer time. Within our models there is no visible trend between the neutron-richness of the models and the amount of ejected ^{56}Ni (as found, e.g. in Nishimura et al. 2017). Rather than the neutron-richness, a more important factor is the explosion energy at the end of the simulations which correlates for our models to the ejected mass of ^{56}Ni . We obtain the relation $M(^{56}\text{Ni}) \approx (0.72 \times E_{51} + 2.31) \times 10^{-2} M_\odot$, which is well in agreement with the observed correlation found within CC-SNe (see e.g. Nomoto et al. 2006, 2013). Except for the weakest magnetized model W, all our models show an exceptional high amount of ^{60}Fe exceeding $10^{-3} M_\odot$ and possibly even growing to $10^{-1} M_\odot$ originating in the moderately neutron-rich conditions with the highest values found in model 35OC-Rp3. Such large values could even be visible as a point source for future telescopes if the event was galactic (Woosley 1997; Diehl 2021).

We stress that the possibility that MR-SNe are directly connected to HNe is not in conflict with the coincident observations of IGRBs and HNe (Nomoto et al. 2006, 2013), since IGRBs may not only be

produced by collapsars (i.e. by central engines hosting a BH). An alternative scenario in the case of MR-SNe, is that the spin down of the protomagnetar acts as central engine of IGRBs (e.g. Metzger, Beniamini & Giannios 2018; AO21). A direct connection to HNe would infer an event rate of $\sim 10^{-5} \text{ yr}^{-1}$ in an average galaxy or one MR-SNe every ~ 700 regular CC-SNe (Podsiadlowski et al. 2004). Given this rate and $M_{A \geq 90} \sim 1 \times 10^{-2} - 4 \times 10^{-2} M_{\odot}$ (for model S, P, and 35OC-Rp3), this fits with the observational determined properties of the dominant r-process site (Hotokezaka, Beniamini & Piran 2018). However, we note that our models synthesize a much larger second to third r-process peak ratio than the solar r-process pattern.

Besides a large amount of ^{56}Ni and a large explosion energy, a high $[\text{Zn}/\text{Fe}]$ ratio has been reported as signature of HNe, which our models reproduce. We applied a simple model for the mixing of the SN ejecta into the ISM to compare these ratios to the observation of metal-poor stars. The obtained ratios are in agreement with observations when assuming a mixing mass around $\sim 10^5 - 10^6 M_{\odot}$ inferred by typical HNe explosion energies of $10^{52} - 10^{53}$ erg (Nomoto et al. 2006, 2013). On the other hand, a high $[\text{Zn}/\text{Fe}]$ ratio is not exclusively obtained by our most magnetized models, but also by the less magnetized ones that are more similar to regular CC-SNe. Indeed also other multidimensional CC-SNe simulations without magnetic fields can obtain high $[\text{Zn}/\text{Fe}]$ ratios (e.g. Eichler et al. 2018; Wanajo et al. 2018; Sieverding et al. 2020; Sandoval et al. 2021). Low $[\text{Zn}/\text{Fe}]$ ratios may therefore be an indication of missing physics in 1D CC-SNe models (see also Sieverding et al. 2020 for a similar conclusion).

Finally, we applied a simplified light curve model based on the spherical expansion of the ejecta and the energy input by radioactive decays to show whether our MR-SN models can reproduce peak luminosities compatible with SLSNe. The model uses the masses of several radioisotopes produced in the explosion. Thus, the resulting light curves depend on whether we use the yields obtained at the final time of the neutrino-MHD simulations, or the (higher) masses obtained by the extrapolation of our results. In the former case, the peak luminosities are in the range of $10^{42} \text{ erg s}^{-1}$ for all models. In the latter case, the luminosity peaks are much broader and with $\sim 10^{43} \text{ erg s}^{-1}$ also brighter. Hence, our results suggest that peak luminosities of the dimmest SLSNe may be produced by the radioactive decay of a blend of isotopes generated explosively during the SN. Larger peak luminosities ($\sim 10^{44} \text{ erg s}^{-1}$ or higher) may require an extra energy release of the central engine (see e.g. OA22), or the interaction of the SN ejecta with the circumstellar medium. We note that the presence of radioactive nuclei different from ^{56}Ni and ^{56}Co can increase the peak luminosity by 10–40 per cent. This increase is mostly powered by the synthesis of neutron-rich ^{66}Cu and ^{66}Ni . However, all our models are dominantly powered by the nuclear decay chain of ^{56}Ni and therefore also the tail of the light curve follows the slope of this decay. This has been shown to be not the case for all SLSNe. The discrepancy can be explained by a central engine as, e.g. the spin-down of a magnetar or the accretion on a central BH. Estimating the effects of such an engine was, however, beyond the scope of our work and leaves room for future investigations.

An investigation of the effect of higher numerical resolution of the neutrino-MHD models would be desirable. A low resolution leads to enhanced numerical diffusion and can, in our environment, smear out the neutron-rich features. Furthermore, the dynamics within the simulation may change significantly (e.g. Nagakura et al. 2019). It is therefore an interesting question to investigate if model S is able to host a more neutron-rich environment when applying a higher resolution. Additionally, longer simulated 3D models would enable

the investigation of long time effects and therefore get more realistic models.

As a final note, we stress that we investigated the nucleosynthesis of some of the most advanced neutrino-MHD models of MR-SNe to date. Our results reinforce the existing possibility stating that MR-SNe are viable candidates for HNe and possibly for SLSNe as well. We furthermore have shown that MR-SNe remain as important candidates for the synthesis of r-process elements in the early Universe.

ACKNOWLEDGEMENTS

We would like to thank Marta Molero and Athanasios Psaltis for fruitful discussions. This work has been supported by the Spanish Ministry of Science, Education and Universities (PGC2018-095984-B-I00, PID2021-127495NB-I00) and the Valencian Community (PROMETEU/2019/071). This article benefited from the ‘ChETEC’ COST Action (CA16117). MG acknowledges support through the Generalitat Valenciana via the grant CIDEGENT/2019/031. AA acknowledges support from the European Research Council under grant EUROPIUM-667912, and from the Deutsche Forschungsgemeinschaft (DFG, German Research Foundation) - Projektnummer 279384907 - SFB 1245 and the State of Hessen within the Research Cluster ELEMENTS (Project ID 500/10.006). MO acknowledges support from the Spanish Ministry of Science via the Ramón y Cajal programme (RYC2018-024938-I).

DATA AVAILABILITY

Yield tables are available in the electronic form of the manuscript online. Other data will be made available upon reasonable requests made to the authors.

REFERENCES

- Allen D. M., Ryan S. G., Rossi S., Beers T. C., Tsangarides S. A., 2012, *A&A*, 548, A34
- Aloy M. Á., Obergaulinger M., 2021, *MNRAS*, 500, 4365
- Aoki W., Norris J. E., Ryan S. G., Beers T. C., Ando H., 2002, *PASJ*, 54, 933
- Aoki W. et al., 2005, *ApJ*, 632, 611
- Aoki W. et al., 2007, *ApJ*, 660, 747
- Aoki W. et al., 2008, *ApJ*, 678, 1351
- Arcones A., Thielemann F. K., 2013, *J. Phys. G: Nucl. Phys.*, 40, 013201
- Arnould M., Goriely S., 2003, *Phys. Rep.*, 384, 1
- Attix F. H., 2004, *Introduction to Radiological Physics and Radiation Dosimetry*. Wiley-VCH Verlag GmbH & Co. KGaA, Weinheim, Germany
- Austin S. M., West C., Heger A., 2017, *ApJ*, 839, L9
- Bandyopadhyay A., Sivarani T., Susmitha A., Beers T. C., Giridhar S., Surya A., Masseron T., 2018, *ApJ*, 859, 114
- Barbuy B., Spite M., Spite F., Hill V., Cayrel R., Plez B., Petitjean P., 2005, *A&A*, 429, 1031
- Barbuy B. et al., 2015, *A&A*, 580, A40
- Barklem P. S. et al., 2005, *A&A*, 439, 129
- Barnes J., Duffell P. C., Liu Y., Modjaz M., Bianco F. B., Kasen D., MacFadyen A. I., 2018, *ApJ*, 860, 38
- Beers T. C., Christlieb N., 2005, *ARA&A*, 43, 531
- Bisnovatyi-Kogan G. S., Popov I. P., Samokhin A. A., 1976, *Ap&SS*, 41, 287
- Bliss J., Arcones A., Qian Y. Z., 2018, *ApJ*, 866, 105
- Bonifacio P. et al., 2009, *A&A*, 501, 519
- Bovard L., Rezzolla L., 2017, *Class. Quantum Gravity*, 34, 215005
- Braithwaite J., 2008, *MNRAS*, 386, 1947
- Brinkman H. E., Doherty C. L., Pols O. R., Li E. T., Côté B., Lugaro M., 2019, *ApJ*, 884, 38

- Brinkman H. E., den Hartog H., Doherty C. L., Pignatari M., Lugaro M., 2021, *ApJ*, 923, 47
- Brown D. et al., 2018, *Nucl. Data Sheets*, 148, 1
- Bruenn S. W. et al., 2016, *ApJ*, 818, 123
- Bugli M., Guilet J., Obergaulinger M., Cerdá-Durán P., Aloy M. A., 2020, *MNRAS*, 492, 58
- Bugli M., Guilet J., Obergaulinger M., 2021, *MNRAS*, 507, 443
- Burrows A., Dessart L., Livne E., Ott C. D., Murphy J., 2007, *ApJ*, 664, 416
- Cain M. et al., 2018, *ApJ*, 864, 43
- Cavallo L., Cescutti G., Matteucci F., 2021, *MNRAS*, 503, 1
- Chan T. K., Theuns T., Bower R., Frenk C., 2021, *MNRAS*, 505, 5784
- Chatzopoulos E., Wheeler J. C., Vinko J., Horvath Z. L., Nagy A., 2013, *ApJ*, 773, 76
- Chen K.-J., Moriya T. J., Woosley S., Sukhbold T., Whalen D. J., Suwa Y., Bromm V., 2017, *ApJ*, 839, 85
- Choplin A., Goriely S., Hirschi R., Tominaga N., Meynet G., 2022, *A&A*, 661, A86
- Christlieb N. et al., 2004, *A&A*, 428, 1027
- Cohen J. G., Huang W., 2009, *ApJ*, 701, 1053
- Cohen J. G., Huang W., 2010, *ApJ*, 719, 931
- Cohen J. G. et al., 2006, *AJ*, 132, 137
- Cohen J. G., Christlieb N., Thompson I., McWilliam A., Shtetman S., Reimers D., Wisotzki L., Kirby E., 2013, *ApJ*, 778, 56
- Cowan J. J. et al., 2002, *ApJ*, 572, 861
- Cowan J. J., Sneden C., Lawler J. E., Aprahamian A., Wiescher M., Langanke K., Martínez-Pinedo G., Thielemann F.-K., 2021, *Rev. Mod. Phys.*, 93, 015002
- Cui W. Y., Sivarani T., Christlieb N., 2013, *A&A*, 558, A36
- Cybur R. H. et al., 2010, *ApJS*, 189, 240
- da Silveira C. R. et al., 2018, *A&A*, 614, A149
- Dado S., Dar A., 2015, *ApJ*, 809, 32
- De Cia A. et al., 2018, *ApJ*, 860, 100
- Dessart L., Hillier D. J., Waldman R., Livne E., Blondin S., 2012, *MNRAS*, 426, L76
- Diehl R., 2013, *Rep. Prog. Phys.*, 76, 026301
- Diehl R., 2021, *Ap&SS*, 366, 104
- Diehl R. et al., 2021, *PASA*, 38, e062
- Doherty C. L., Gil-Pons P., Lau H. H. B., Lattanzio J. C., Siess L., 2014, *MNRAS*, 437, 195
- Eichler M. et al., 2018, *J. Phys. G: Nucl. Phys.*, 45, 014001
- Eichler M., Sayar W., Arcones A., Rauscher T., 2019, *ApJ*, 879, 47
- Eriksen K. A., Arnett D., McCarthy D. W., Young P., 2009, *ApJ*, 697, 29
- Ezzeddine R. et al., 2019, *ApJ*, 876, 97
- Farouqi K., Thielemann F.-K., Rosswog S., Kratz K.-L., 2021, *A&A*, 663, A70
- Fehlberg E., 1969, Technical Report R-315, Low-order Classical Runge-Kutta Formulas with StepSize Control and their Application to some Heat Transfer Problems. NASA, Washington, DC
- Frebel A., Simon J. D., Geha M., Willman B., 2010, *ApJ*, 708, 560
- Frebel A., Simon J. D., Kirby E. N., 2014, *ApJ*, 786, 74
- Freiburghaus C., Rembges J. F., Rauscher T., Kolbe E., Thielemann F. K., Kratz K. L., Pfeiffer B., Cowan J. J., 1999, *ApJ*, 516, 381
- Fröhlich C. et al., 2006, *ApJ*, 637, 415
- Fujimoto S.-i., Nishimura N., Hashimoto M.-a., 2008, *ApJ*, 680, 1350
- Gal-Yam A., 2012, *Science*, 337, 927
- Gal-Yam A., 2019, *ARA&A*, 57, 305
- Gilmore G., Norris J. E., Monaco L., Yong D., Wyse R. F. G., Geisler D., 2013, *ApJ*, 763, 61
- Grebenev S. A., Lutovinov A. A., Tsygankov S. S., Winkler C., 2012, *Nature*, 490, 373
- Griffiths A., Meynet G., Eggenberger P., Moyano F., Aloy M. A., 2022, *A&A*, 665, A147
- Grimmett J. J., Heger A., Karakas A. I., Müller B., 2018, *MNRAS*, 479, 495
- Grimmett J. J., Karakas A. I., Heger A., Müller B., West C., 2020, *MNRAS*, 496, 4987
- Grimmett J. J., Müller B., Heger A., Banerjee P., Obergaulinger M., 2021, *MNRAS*, 501, 2764
- Gull M. et al., 2018, *ApJ*, 862, 174
- Halevi G., Mösta P., 2018, *MNRAS*, 477, 2366
- Hamuy M., 2003, *ApJ*, 582, 905
- Hansen T. et al., 2015, *ApJ*, 807, 173
- Hansen T. T. et al., 2017, *ApJ*, 838, 44
- Harris J. A., Hix W. R., Chertkow M. A., Lee C. T., Lentz E. J., Messer O. E. B., 2017, *ApJ*, 843, 2
- Hill V. et al., 2002, *A&A*, 387, 560
- Hirai Y., Saitoh T. R., Ishimaru Y., Wanajo S., 2018, *ApJ*, 855, 63
- Hollek J. K., Frebel A., Roederer I. U., Sneden C., Shetrone M., Beers T. C., Kang S.-j., Thom C., 2011, *ApJ*, 742, 54
- Holmbeck E. M. et al., 2018, *ApJ*, 859, L24
- Holmbeck E. M., Frebel A., McLaughlin G. C., Mumpower M. R., Sprouse T. M., Surman R., 2019, *ApJ*, 881, 5
- Honda S., Aoki W., Ishimaru Y., Wanajo S., 2007, *ApJ*, 666, 1189
- Honda S., Aoki W., Beers T. C., Takada-Hidai M., 2011, *ApJ*, 730, 77
- Horowitz C. J. et al., 2019, *J. Phys. G: Nucl. Phys.*, 46, 083001
- Hotokezaka K., Beniamini P., Piran T., 2018, *Int. J. Mod. Phys.*, 27, 1842005
- Insera C. et al., 2013a, *A&A*, 555, A142
- Insera C. et al., 2013b, *ApJ*, 770, 128
- Ishigaki M. N., Aoki W., Chiba M., 2013, *ApJ*, 771, 67
- Ivans I. I., Sneden C., James C. R., Preston G. W., Fulbright J. P., Höflich P. A., Carney B. W., Wheeler J. C., 2003, *ApJ*, 592, 906
- Iwamoto K. et al., 1998, *Nature*, 395, 672
- Izzo L. et al., 2019, *Nature*, 565, 324
- Jacobson H. R. et al., 2015, *ApJ*, 807, 171
- Jerkstrand A., Maeda K., Kawabata K. S., 2020, *Science*, 367, 415
- Ji A. P., Frebel A., 2018, *ApJ*, 856, 138
- Ji A. P., Simon J. D., Frebel A., Venn K. A., Hansen T. T., 2019, *ApJ*, 870, 83
- Jones S. W. et al., 2019, *MNRAS*, 485, 4287
- Just O., Obergaulinger M., Janka H.-T., 2015, *MNRAS*, 453, 3386
- Just O., Aloy M. A., Obergaulinger M., Nagataki S., 2022a, *ApJL*, 934, L30
- Just O., Goriely S., Janka H. T., Nagataki S., Bauswein A., 2022b, *MNRAS*, 509, 1377
- Karakas A. I., 2010, *MNRAS*, 403, 1413
- Kasen D., Bildsten L., 2010, *ApJ*, 717, 245
- Keszthelyi Z., Meynet G., Georgy C., Wade G. A., Petit V., David-Uraz A., 2019, *MNRAS*, 485, 5843
- Kirby E. N., Cohen J. G., 2012, *AJ*, 144, 168
- Kirby E. N., Cohen J. G., Simon J. D., Guhathakurta P., Thygesen A. O., Duggan G. E., 2017, *ApJ*, 838, 83
- Kobayashi C., Umeda H., Nomoto K., Tominaga N., Ohkubo T., 2006, *ApJ*, 653, 1145
- Kobayashi C., Karakas A. I., Lugaro M., 2020, *ApJ*, 900, 179
- Komissarov S. S., 1999, *MNRAS*, 308, 1069
- Kuroda T., Arcones A., Takiwaki T., Kotake K., 2020, *ApJ*, 896, 102
- Lai D. K., Bolte M., Johnson J. A., Lucatello S., Heger A., Woosley S. E., 2008, *ApJ*, 681, 1524
- Langanke K., Kolbe E., 2001, *At. Data Nucl. Data Tables*, 79, 293
- Langanke K., Martínez-Pinedo G., 2001, *At. Data Nucl. Data Tables*, 79, 1
- Lawson T. V., Pignatari M., Stancliffe R. J., den Hartogh J., Jones S., Fryer C. L., Gibson B. K., Lugaro M., 2022, *MNRAS*, 511, 886
- LeBlanc J. M., Wilson J. R., 1970, *ApJ*, 161, 541
- Leismann T., Antón L., Aloy M. A., Müller E., Martí J. M., Miralles J. A., Ibáñez J. M., 2005, *A&A*, 436, 503
- Li H.-N., Zhao G., Christlieb N., Wang L., Wang W., Zhang Y., Hou Y., Yuan H., 2015, *ApJ*, 798, 110
- Limongi M., Chieffi A., 2006, *ApJ*, 647, 483
- Limongi M., Chieffi A., 2012, *ApJS*, 199, 38
- Lind K. R., Payne D. G., Meier D. L., Blandford R. D., 1989, *ApJ*, 344, 89
- Lodders K., Palme H., Gail H. P., 2009, *Landolt B'ornstein*, 4B, 712
- Ludwig P. et al., 2016, *Proc. Natl. Acad. Sci.*, 113, 9232
- MacFadyen A. I., Woosley S. E., 1999, *ApJ*, 524, 262
- McLaughlin G. C., Surman R., 2005, *Nucl. Phys. A*, 758, 189
- Maeda K., Nomoto K., 2003, *ApJ*, 598, 1163
- Maeder A., Meynet G., 2003, *A&A*, 411, 543
- Maeder A., Meynet G., 2004, *A&A*, 422, 225
- Maeder A., Meynet G., 2005, *A&A*, 440, 1041
- Maeder A., Meynet G., 2012, *Rev. Mod. Phys.*, 84, 25

- Magg M. et al., 2020, *MNRAS*, 498, 3703
- Magkotsios G., Timmes F. X., Wiescher M., 2011, *ApJ*, 741, 78
- Mardini M. K., Placco V. M., Taani A., Li H., Zhao G., 2019, *ApJ*, 882, 27
- Martin D., Perego A., Kastaun W., Arcones A., 2018, *Class. Quantum Gravity*, 35, 034001
- Masada Y., Takiwaki T., Kotake K., Sano T., 2012, *ApJ*, 759, 110
- Mashonkina L., Christlieb N., Barklem P. S., Hill V., Beers T. C., Velichko A., 2010, *A&A*, 516, A46
- Mashonkina L., Christlieb N., Eriksson K., 2014, *A&A*, 569, A43
- Masseron T. et al., 2006, *A&A*, 455, 1059
- Matsumoto J., Asahina Y., Takiwaki T., Kotake K., Takahashi H. R., 2022, *MNRAS*, 516, 1752–1767
- Mazzali P. A., McFadyen A. I., Woosley S. E., Pian E., Tanaka M., 2014, *MNRAS*, 443, 67
- Meier D. L., Epstein R. I., Arnett W. D., Schramm D. N., 1976, *ApJ*, 204, 869
- Metzger B. D., Margalit B., Kasen D., Quataert E., 2015, *MNRAS*, 454, 3311
- Metzger B. D., Beniamini P., Giannios D., 2018, *ApJ*, 857, 95
- Meyer B. S., 1994, *ARA&A*, 32, 153
- Meyer B. S., 2002, *Phys. Rev. Lett.*, 89, 231101
- Miller J. M., Sprouse T. M., Fryer C. L., Ryan B. R., Dolence J. C., Mumpower M. R., Surman R., 2020, *ApJ*, 902, 66
- Mishenina T. et al., 2017, *MNRAS*, 469, 4378
- Moriya T. J., Sorokina E. I., Chevalier R. A., 2018, *Space Sci. Rev.*, 214, 59
- Mösta P. et al., 2014, *ApJ*, 785, L29
- Mösta P., Ott C. D., Radice D., Roberts L. F., Schnetter E., Haas R., 2015, *Nature*, 528, 376
- Mösta P., Roberts L. F., Halevi G., Ott C. D., Lippuner J., Haas R., Schnetter E., 2018, *ApJ*, 864, 171
- Mueller E., Hillebrandt W., 1979, *A&A*, 80, 147
- Müller B., Varma V., 2020, *MNRAS*, 498, L109
- Nadyozhin D. K., 1994, *ApJS*, 92, 527
- Nadyozhin D. K., Deputovich A. Y., 2002, *A&A*, 386, 711
- Nagakura H., Burrows A., Radice D., Vartanyan D., 2019, *MNRAS*, 490, 4622
- Nagataki S., Hashimoto M.-a., Sato K., Yamada S., 1997, *ApJ*, 486, 1026
- Nagataki S., Hashimoto M.-a., Sato K., Yamada S., Mochizuki Y. S., 1998, *ApJ*, 492, L45
- Nakamura K., Takiwaki T., Kotake K., 2019, *PASJ*, 71, 98
- Nicholl M., 2021, *Astron. Geophys.*, 62, 5.34
- Nicholl M. et al., 2014, *MNRAS*, 444, 2096
- Nicholl M. et al., 2015, *MNRAS*, 452, 3869
- Nicholl M., Guillochon J., Berger E., 2017, *ApJ*, 850, 55
- Nishimura S., Kotake K., Hashimoto M.-a., Yamada S., Nishimura N., Fujimoto S., Sato K., 2006, *ApJ*, 642, 410
- Nishimura N., Takiwaki T., Thielemann F.-K., 2015, *ApJ*, 810, 109
- Nishimura N., Sawai H., Takiwaki T., Yamada S., Thielemann F.-K., 2017, *ApJ*, 836, L21
- Nomoto K., 2017, Springer International Publishing, Cham (Switzerland), Nucleosynthesis in Hypernovae Associated with Gamma-Ray Bursts. p. 1931
- Nomoto K., Tominaga N., Umeda H., Kobayashi C., Maeda K., 2006, *Nucl. Phys. A*, 777, 424
- Nomoto K., Kobayashi C., Tominaga N., 2013, *ARA&A*, 51, 457
- Obergaulinger M., Aloy M. Á., 2017, *MNRAS*, 469, L43
- Obergaulinger M., Aloy M. Á., 2020, *MNRAS*, 492, 4613
- Obergaulinger M., Aloy M. Á., 2021, *MNRAS*, 503, 4942
- Obergaulinger M., Aloy M. Á., 2022, *MNRAS*, 512, 2489
- Obergaulinger M., Cerdá-Durán P., Müller E., Aloy M. A., 2009, *A&A*, 498, 241
- Panov I. V., Kolbe E., Pfeiffer B., Rauscher T., Kratz K.-L., Thielemann F.-K., 2005, *Nucl. Phys. A*, 747, 633
- Panov I. V., Korneev I. Y., Rauscher T., Martínez-Pinedo G., Kelić-Heil A., Zinner N. T., Thielemann F.-K., 2010, *A&A*, 513, A61
- Pellin M. J. et al., 2006, in Mackwell S., Stansbery E., eds, 37th Annual Lunar and Planetary Science Conference, Lunar and Planetary Science Conference. Lunar and Planetary Science Conference, p.2041
- Perego A., Rosswog S., Cabezón R. M., Korobkin O., Käppeli R., Arcones A., Liebendörfer M., 2014, *MNRAS*, 443, 3134
- Pignatari M., Göbel K., Reifarth R., Travaglio C., 2016, *Int. J. Mod. Phys.*, 25, 1630003
- Placco V. M. et al., 2015, *ApJ*, 812, 109
- Placco V. M., Beers T. C., Reggiani H., Meléndez J., 2016, *ApJ*, 829, L24
- Podsiadlowski P., Mazzali P. A., Nomoto K., Lazzati D., Cappellaro E., 2004, *ApJ*, 607, L17
- Purandardas M., Goswami A., Goswami P. P., Shejeelammal J., Masseron T., 2019, *MNRAS*, 486, 3266
- Qian Y. Z., Woosley S. E., 1996, *ApJ*, 471, 331
- Quimby R. M. et al., 2011, *Nature*, 474, 487
- Rayet M., Arnould M., Hashimoto M., Prantzos N., Nomoto K., 1995, *A&A*, 298, 517
- Reichert M., Hansen C. J., Hanke M., Skúladóttir Á., Arcones A., Grebel E. K., 2020, *A&A*, 641, A127
- Reichert M., Obergaulinger M., Eichler M., Aloy M. Á., Arcones A., 2021a, *MNRAS*, 501, 5733
- Reichert M., Hansen C. J., Arcones A., 2021b, *ApJ*, 912, 157
- Rembiasz T., Obergaulinger M., Cerdá-Durán P., Müller E., Aloy M. A., 2016, *MNRAS*, 456, 3782
- Roederer I. U., Kratz K.-L., Frebel A., Christlieb N., Pfeiffer B., Cowan J. J., Sneden C., 2009, *ApJ*, 698, 1963
- Roederer I. U., Cowan J. J., Karakas A. I., Kratz K.-L., Lugaro M., Simmerer J., Farouqi K., Sneden C., 2010, *ApJ*, 724, 975
- Roederer I. U., Preston G. W., Thompson I. B., Shtetman S. A., Sneden C., Burley G. S., Kelson D. D., 2014, *AJ*, 147, 136
- Roriz M., Pereira C. B., Drake N. A., Roig F., Silva J. V. S., 2017, *MNRAS*, 472, 350
- Ryan S. G., Norris J. E., Beers T. C., 1996, *ApJ*, 471, 254
- Sakari C. M. et al., 2018, *ApJ*, 868, 110
- Sandoval M. A., Hix W. R., Messer O. E. B., Lentz E. J., Harris J. A., 2021, *ApJ*, 921, 113
- Sato T. et al., 2021, *Nature*, 592, 537
- Schönrich R. A., Weinberg D. H., 2019, *MNRAS*, 487, 580
- Seitenzahl I. R., Taubenberger S., Sim S. A., 2009, *MNRAS*, 400, 531
- Seitenzahl I. R., Timmes F. X., Magkotsios G., 2014, *ApJ*, 792, 10
- Shingles L. J. et al., 2020, *MNRAS*, 492, 2029
- Siegel D. M., Barnes J., Metzger B. D., 2019, *Nature*, 569, 241
- Siegel D. M., Agarwal A., Barnes J., Metzger B. D., Renzo M., Villar V. A., 2021, preprint ([arXiv:2111.03094](https://arxiv.org/abs/2111.03094))
- Sieverding A., Müller B., Qian Y. Z., 2020, *ApJ*, 904, 163
- Siqueira-Mello C., Andrievsky S. M., Barbuy B., Spite M., Spite F., Korotin S. A., 2015, *A&A*, 584, A86
- Sivarani T. et al., 2006, *A&A*, 459, 125
- Skúladóttir Á., Tolstoy E., Salvadori S., Hill V., Pettini M., Shetrone M. D., Starkenburg E., 2015, *A&A*, 574, A129
- Sneden C., Cowan J. J., Lawler J. E., 2003, *Nucl. Phys. A*, 718, 29
- Soker N., 2022, *ApJ*, 935, 108
- Soker N., Gilkis A., 2017, *ApJ*, 851, 95
- Suda T. et al., 2017, *PASJ*, 69, 76
- Sukhbold T., Ertl T., Woosley S. E., Brown J. M., Janka H. T., 2016, *ApJ*, 821, 38
- Surman R., McLaughlin G. C., 2004, *ApJ*, 603, 611
- Surman R., McLaughlin G. C., Hix W. R., 2006, *ApJ*, 643, 1057
- Suwa Y., Takiwaki T., Kotake K., Sato K., 2007, *PASJ*, 59, 771
- Suwa Y., Tominaga N., Maeda K., 2019, *MNRAS*, 483, 3607
- Symbalisty E. M. D., 1984, *ApJ*, 285, 729
- Taddia F. et al., 2016, *A&A*, 588, A5
- Taddia F. et al., 2019, *A&A*, 621, A71
- Takahashi K., Witt J., Janka H. T., 1994, *A&A*, 286, 857
- Thielemann F.-K., Eichler M., Panov I. V., Wehmeyer B., 2017, *Annu. Rev. Nucl. Part. Sci.*, 67, 253
- Thielemann F.-K., Isern J., Perego A., von Ballmoos P., 2018, *Space Sci. Rev.*, 214, 62

- Tominaga N., Umeda H., Nomoto K., 2007, *ApJ*, 660, 516
 Trappitsch R. et al., 2018, *ApJ*, 857, L15
 Travaglio C., Rauscher T., Heger A., Pignatari M., West C., 2018, *ApJ*, 854, 18
 Tsujimoto T., Nishimura N., 2018, *ApJ*, 863, L27
 Umeda H., Nomoto K., 2002, *ApJ*, 565, 385
 van de Voort F., Pakmor R., Grand R. J. J., Springel V., Gómez F. A., Marinacci F., 2020, *MNRAS*, 494, 4867
 van de Voort F., Pakmor R., Bieri R., Grand R. J. J., 2022, *MNRAS*, 512, 5258
 Vance G. S., Young P. A., Fryer C. L., Ellinger C. I., 2020, *ApJ*, 895, 82
 Varma V., Müller B., 2021, *MNRAS*, 504, 636
 Varma V., Mueller B., Schneider F. R. N., 2022, preprint (arXiv:2204.11009)
 Wallner A. et al., 2016, *Nature*, 532, 69
 Wanajo S., Müller B., Janka H.-T., Heger A., 2018, *ApJ*, 852, 40
 Wang W., Li Z., 2016, *ApJ*, 825, 102
 Wang W. et al., 2020, *ApJ*, 889, 169
 Westin J., Sneden C., Gustafsson B., Cowan J. J., 2000, *ApJ*, 530, 783
 Wheeler J. C., Cowan J. J., Hillebrandt W., 1998, *ApJ*, 493, L101
 Wheeler J. C., Kagan D., Chatzopoulos E., 2015, *ApJ*, 799, 85
 Winteler C., Käppeli R., Perego A., Arcones A., Vasset N., Nishimura N., Liebendörfer M., Thielemann F.-K., 2012, *ApJ*, 750, L22
 Witt M. et al., 2021, *ApJ*, 921, 19
 Wollaeger R. T., Hungerford A. L., Fryer C. L., Wollaber A. B., van Rossum D. R., Even W., 2017, *ApJ*, 845, 168
 Woosley S. E., 1997, *ApJ*, 476, 801
 Woosley S. E., 2010, *ApJ*, 719, L204
 Woosley S. E., Bloom J. S., 2006, *ARA&A*, 44, 507
 Woosley S. E., Heger A., 2006, *ApJ*, 637, 914
 Woosley S. E., Wilson J. R., Mathews G. J., Hoffman R. D., Meyer B. S., 1994, *ApJ*, 433, 229
 Woosley S. E., Heger A., Weaver T. A., 2002, *Rev. Mod. Phys.*, 74, 1015
 Wu M.-R., Banerjee P., 2022, *AAPPS Bulletin*, 32, 19
 Wu M.-R., Barnes J., Martínez-Pinedo G., Metzger B. D., 2019, *Phys. Rev. Lett.*, 122, 062701
 Yong D. et al., 2021, *Nature*, 595, 223

SUPPORTING INFORMATION

Supplementary data are available at [MNRAS](https://www.mnras.org/online) online.

Table D1. Yield table for model O after 1 Gyr.

Table D2. Same as Table D1, but for model W.

Table D3. Same as Table D1, but for model P.

Table D4. Same as Table D1, but for model S.

Table D5. Same as Table D1, but for model 35OC-R_SN.

Table D6. Same as Table D1, but for model 35OC-Rp3.

Please note: Oxford University Press is not responsible for the content or functionality of any supporting materials supplied by the authors. Any queries (other than missing material) should be directed to the corresponding author for the article.

APPENDIX A: TRACER INTEGRATION

The tracer particles are calculated backwards in time using snapshots of the neutrino-MHD simulations. These snapshots are available every millisecond. To integrate the trajectories backwards in time, we employ the so called Runge–Kutta–Fehlberg method (RKF45; Fehlberg 1969). This method employs a fourth order Runge–Kutta algorithm with a fifth order error estimate, allowing for an automated step size control. Our implementation includes an individual step size for every tracer and, if necessary, interpolate linearly in time between the snapshots of the simulations. In the following, we briefly discuss the impact of the time resolution of the checkpoint files.

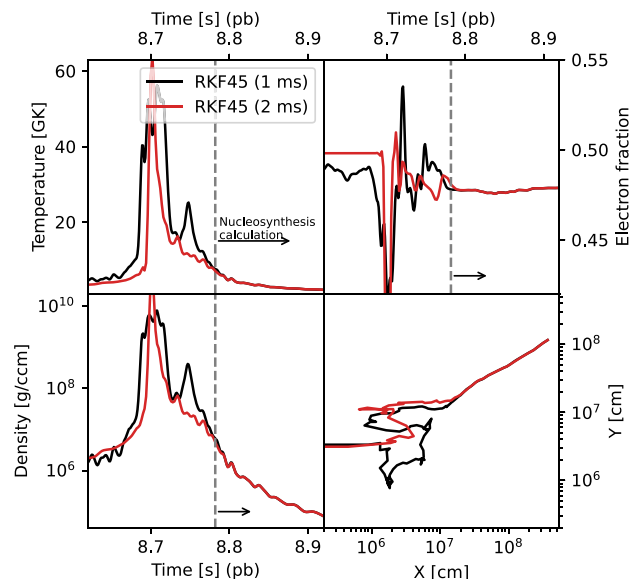


Figure A1. Impact on different properties (see vertical labels) of the time resolution for the checkpoint files, as well as different integration schemes. The dashed line shows the point in time when the tracer falls below 7 GK. The lower right-hand panel shows the projection of the trajectories on the XY-plane. The largest differences in the trajectory happen relatively close to the compact remnant. Above a few 10^7 cm the trajectories run in parallel.

To test if the time resolution of the checkpoint files is sufficiently high, we computed tracers based on the simulation data with a time sampled every millisecond and every two milliseconds. In between two checkpoint files, the velocity field is linearly interpolated. In regions close to the centre of the exploding star or in turbulent flows with rapidly varying velocity fields, this can lead to diverging trajectories. The impact can exemplarily be seen in Fig. A1, where we have picked a representative tracer of model 35OC-Rp3.

We emphasize that the integration is performed backward in time with the initial conditions set at $t \approx 8.96$ s. The two versions of the tracer (black and red lines) agree very well for $t \geq 8.78$ s, which corresponds to the time after they are ejected from the vicinity of the PNS (distances from the centre of ≥ 200 km). Before that point, the tracers are in a region where the velocity field varies strongly with time and position causing the positions and physical properties of the two calculations to disagree considerably. In practice, this disagreement has little impact on the nucleosynthesis because during the entire period both versions of the tracer possess sufficiently high temperatures, $T > 7$ GK, for NSE to apply. Both drop out of NSE after this phase and at almost the same positions and with almost identical density, temperature, and Y_e . Since the subsequent nucleosynthesis is insensitive to the history of a tracer prior to leaving NSE, the final yields of both tracer calculations are the same. To exploit this insensitivity, it is important to integrate the tracers backward in time. The forward integration of a tracer starting in (or passing through) the turbulent velocity field would introduce a sensitivity of the post-NSE conditions to the precise initial positions and prevent the same good agreement.

To test the impact on the integrated yields, we calculate model O twice, one time with a snapshot time resolution of 1 ms and once with a resolution of 2 ms (Fig. A2). There are small differences visible, most dominant around $A \sim 90$. However, these differences are negligible and smaller than other typical errors associated to uncertainties of nuclear reaction rates or of astrophysical origin.

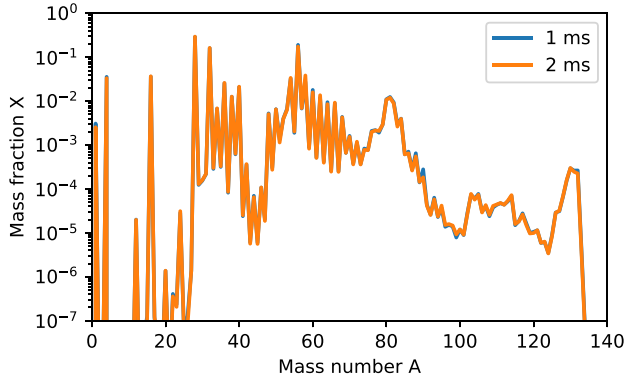


Figure A2. Final nucleosynthetic yields for model O with varied checkpoint resolution of the neutrino-MHD simulation.

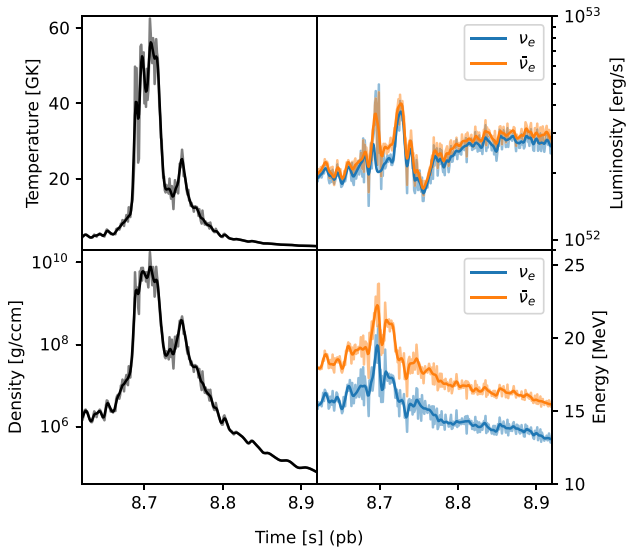


Figure A3. Impact of the applied low-pass filter on the temperature (upper left), density (lower left), neutrino luminosities (upper right), and neutrino energies (lower right) of an example trajectory. The thick solid lines correspond to the filtered data, and the (background) softer and more variable lines to the unfiltered ones.

In order to speed up the nucleosynthesis calculation, we reduce the noise of the temperature, density, and neutrino quantities. This noise stems from interpolation artifacts and small uncertainties of the advection scheme, especially in the central region close to the PNS. We apply a low-pass filter on all tracked quantities. We choose the threshold frequency of the low-pass filter fairly high and, as a consequence, we mainly smooth the neutrino luminosities and energies (see Fig. A3).

APPENDIX B: TRACER SELECTION

Our neutrino-MHD models are the first ones that combine accurate neutrino transport, full 3D, and long evolution of the order of seconds. As a consequence of the long evolution times, also the amount of ejected mass is fairly large ($\sim 10^{-1} - 1 M_{\odot}$; Table 1). This is one to two orders of magnitude larger than previous 3D simulations (cf. $\sim 7 \times 10^{-3} M_{\odot}$ in Winteler et al. 2012 or $\sim 3 \times 10^{-2} M_{\odot}$ in Mösta et al. 2018) and poses a computational challenge, since for an accurate estimate of the nuclear yields around one million tracer particles per model are necessary (Table 1). The average computation time of

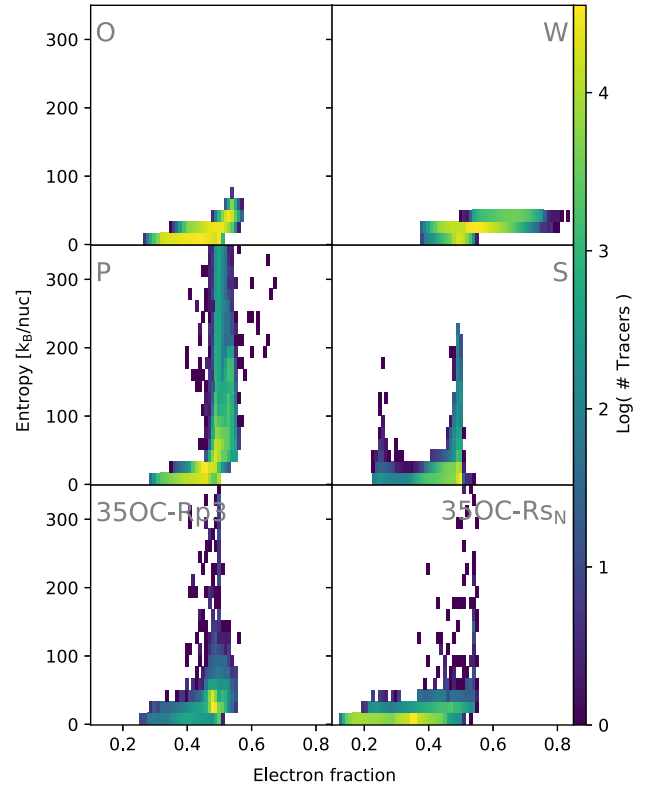


Figure B1. Entropy versus electron fraction at 7 GK. Each panel corresponds to a different model (see legends). The colour indicates the number of tracer particles in the individual bin. Notice that the mass distribution will differ because the tracers have different masses.

the nucleosynthesis of a single tracer particle lies around ~ 20 min on one standard computing core (22 min for model 350C-Rp3). An adequate resolution of tracer particles in our 3D models requires $\sim 10^6$ tracer particles (Table 1). The calculation of one model would therefore result in $\sim 3 \times 10^5$ core hours. This is less than the neutrino-MHD calculation of the 3D models itself ($\sim 10^7$ core hours). Anyway, the reported numbers show that a nucleosynthesis calculation of all tracer particles would be extremely computational demanding, and we therefore select representative conditions and only calculate a subset of tracer particles.

Tracer particles that reach maximum temperatures of at least 7 GK attain nuclear statistical equilibrium (NSE). In a first step, we therefore divide all tracer particles in hot and cold ones, depending respectively on whether their maximum temperatures reach $T_{\max} \geq 7$ GK or not. Since the entropy and electron fraction dominantly influence the composition in the equilibrium for Lagrangian tracers with $T_{\max} \geq 7$ GK, it is useful to group them in bins of S and Y_e for a fixed reference temperature (7 GK in our case; see e.g. Freiburghaus et al. 1999; Thielemann et al. 2017; Mösta et al. 2018; Reichert et al. 2021a). The bin size and the number of calculated tracer particles per bin was chosen from the experience gained with model 350C-Rp3 (0.01 in electron fraction and $15 k_B/\text{nuc}$ in specific entropy). In a Cartesian tessellation of the (S, Y_e) phase space, most of the elements of the partition do not contain any tracer (white areas in Fig. B1). For the chosen partition size, only $N_b = 198$ bins contain hot tracers in the case of model 350C-Rp3, as can be seen in the coloured rectangles of Fig. B1. Other models display different thermodynamic conditions, noticeable in the diversity of morphologies in the corresponding entropy-electron fraction plane.

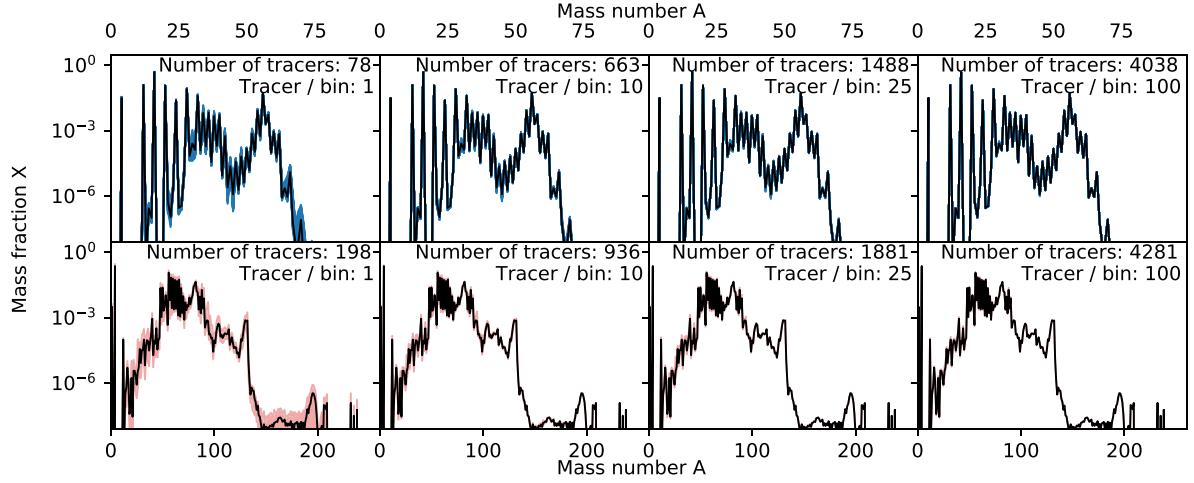


Figure B2. Obtained nucleosynthetic yield for different number of tracers per bin in model 35OC-Rp3. In the upper row, we consider the cold subset of tracers (with a maximum temperature below 7 GK) and, in the lower row, the hot subset (with a maximum temperature above 7 GK). The total number of bins containing tracers in the (S, Y_e) tessellation of the phase space are $N_b = 78$ and $N_b = 198$ for the cold and hot subsets, respectively. From the left to the right column we randomly pick an increasing number of *representative* tracers in each bin, N_{rep} . We recall that some bins may contain a number of Lagrangian tracers smaller than N_{rep} . To quantify the variability in the random choice of tracers inside a bin, we repeat the random choice of tracers within each bin 100 times. For each of the repetitions, we compute the mass fraction of the nucleosynthetic yields as a function of the mass number. The minimum and maximum mass fractions obtained by the former procedure at each mass number are registered, and shown by bands for cold tracers in blue (upper panel) and hot tracers in red (lower panel). The mass-fraction including all available tracer particles of the model is displayed with a solid black line. A good agreement can be obtained when selecting 25 tracer particles per bin.

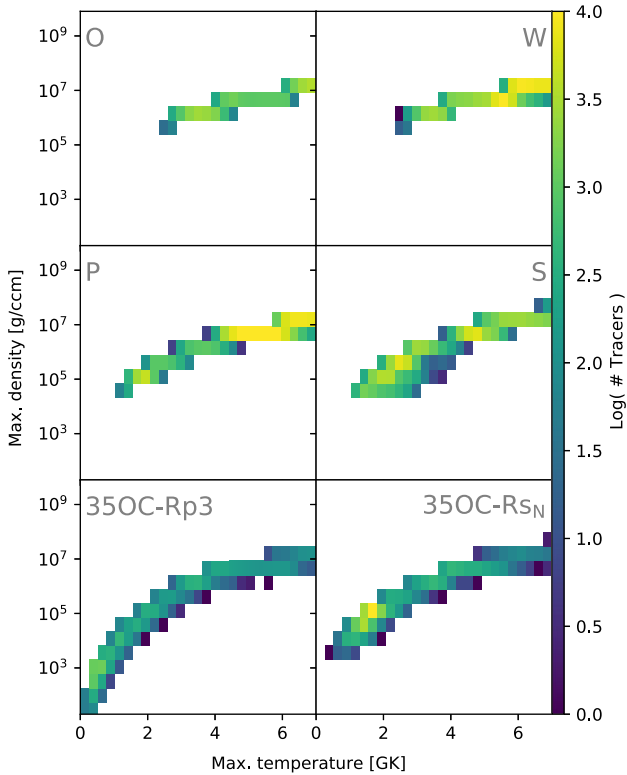


Figure B3. Maximum density versus maximum temperature distribution of tracer particles colder than 7 GK. Notice that the mass distribution will differ because the tracers have different masses.

In order to reduce the total number of tracers to be processed, we randomly select a number N_{rep} of *representative* Lagrangian markers per (S, Y_e) bin at $T = 7$ GK. In Fig. B2 we show the obtained nucleosynthetic yields for various choices of N_{rep} for model 35OC-

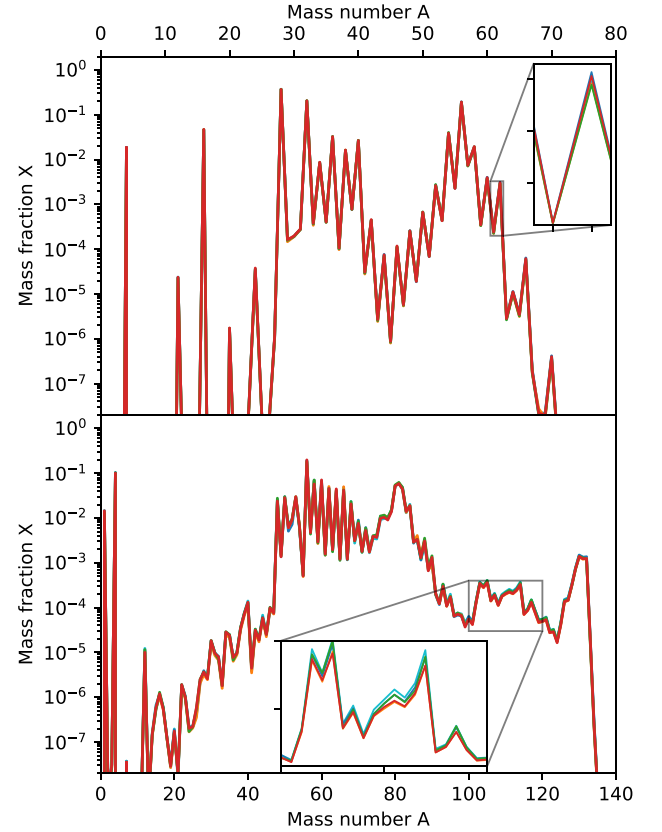


Figure B4. Different nucleosynthetic result for five times randomly chosen trajectories of the individual bins. The upper panel shows the result for cold trajectories, while the lower one shows the result for hot trajectories. Insets show magnifications of some regions, displaying the small scattering of the nucleosynthetic predictions among different random realizations of the choice of representative tracers in model O.

Rp3. For $N_{\text{rep}} = 25$ we find a good trade-off between employing the minimum possible total number of tracers and reducing the scattering of the nucleosynthetic yields prediction induced by the random selection of Lagrangian particles inside each bin. In most (S, Y_e) bins, the number of tracers is significantly larger than N_{rep} . However, if the bin contains less than N_{rep} tracers, we calculate the nucleosynthetic yields for all tracers in the bin. This leads to a sufficient agreement between the overall yields and our representatives in model 35OC-Rp3 (lower panel of Fig. B2). Employing this procedure, there is a reduction by a factor $\gtrsim 100$ of the processing time and memory/storage requests of hot tracers.

For tracers with $T_{\text{max}} < 7$ GK the assumption of NSE does not necessarily hold. Instead, the maximum temperature and density is a good indicator of the location in the progenitor and the final nucleosynthetic pattern (see e.g. Vance et al. 2020; Reichert et al. 2021a). Similarly to the case of the hot tracers, we tessellate the ($T_{\text{max}}, \rho_{\text{max}}$) phase space into bins. Out of this tessellation, only $N_b = 78$ bins contain tracers (coloured rectangles in Fig. B3). Analogously to hot tracers, for cold ones, we have experienced picking only N_{rep} per bin in model 35OC-Rp3, again finding that $N_{\text{rep}} = 25$ suffices for a convergent estimate of the nucleosynthetic yields (Fig. B2; upper panels).

Also for the cold tracers, the selection of only a few representatives for individual conditions decreases the necessary amount of calculated tracer particles and therefore the computational cost by a factor of around 500 (Table 1) without loosing accuracy (upper panel of Fig. B2).

We tested the selection criterion explained above also in the 3D model O. We have calculated it five times, always choosing randomly different representative tracers. The result agrees very well with negligible deviations (Fig. B4).

APPENDIX C: PROTON-RICH OUTFLOW

While studies of MR-SNe usually focus on the outflow of neutron-rich material and the synthesized heavy elements, we take the opportunity to shortly discuss also the proton-rich (i.e. $Y_e > 0.5$) outflow of our models. This proton-rich outflow is a novelty of our studies (see also Reichert et al. 2021a) and has not yet been observed in other nucleosynthesis studies (cf. Nishimura et al. 2006; Winteler et al. 2012; Nishimura et al. 2015, 2017; Mösta et al. 2018). One of the main differences between the underlying hydrodynamic simulations here and in other studies is the more reliable M1 neutrino transport scheme and the longer simulation times (Obergaullinger & Aloy 2017, 2020, 2021; Aloy & Obergaullinger 2021). With the exception of model W, the proton-rich ejecta is located in the centre of the jet (Figs 1 and 10). In total, the ejected mass of proton-rich material is smaller than $< 8 \times 10^{-2} M_{\odot}$. However, this can make up around to 7, 11, 0.8, 5, 0.03, and 0.8 per cent of the total ejected mass of models O, W, P, 35OC-Rp3, S, and 35OC-Rs_N, respectively. The stronger the magnetic field of the model, the lower is the fraction of proton-rich matter in the ejecta. Furthermore, we note that a more oblate PNS leads to more extreme values of the electron fractions in the jet. This phenomena is more common within the 2D axisymmetric models. The synthesized elements in proton-rich ejecta are distributed around a peak of ^{56}Ni , but can also contribute to the synthesis of so called p-nuclei such as ^{74}Se , ^{78}Kr , ^{84}Sr , or ^{92}Mo . However, p-nuclei are only synthesized in a non-negligible amount in model W, the model that is most close to a regular CC-SNe. Additionally, given the expected rareness of MR-SNe in contrast to regular SNe, the galactic contribution to p-nuclei in the lower mass range ($A < 100$) from

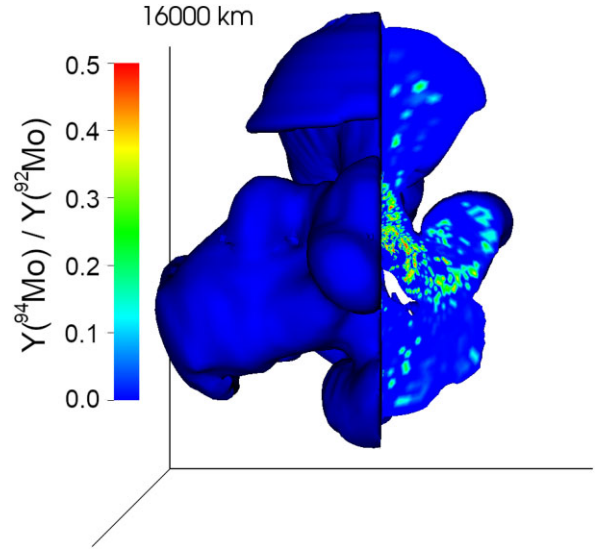


Figure C1. Spatial distribution of the $Y(^{94}\text{Mo})/Y(^{92}\text{Mo})$ ratio at the end of the simulation in model W. Regions with $Y(^{92}\text{Mo}) = 0$ or $Y(^{94}\text{Mo}) = 0$ are shown as blue colours.

the proton-rich outflow of MR-SNe may therefore be negligible. Therefore, we focus only shortly on model W in the following. For this model, we find proton-rich nuclei up to $A \sim 100$ (cf. Bliss, Arcones & Qian 2018; Eichler et al. 2018), heavier ones may get formed by the p/γ -process (see e.g. Rayet et al. 1995; Arnould & Goriely 2003; Pignatari et al. 2016; Travaglio et al. 2018; Choplin et al. 2022, and references therein). However, the composition within our progenitor is not detailed enough to investigate this process.

Despite the total ejected mass of p-nuclei, isotopic ratios can give interesting clues about the formation of elements. An interesting isotopic ratio of a proton-rich isotope is given by $Y(^{94}\text{Mo})/Y(^{92}\text{Mo})$. This ratio can be determined within meteorites, so called SiC grains of type X which are thought to be formed from the ejecta of CC-SNe. The measured ratios of the grains and also of the sun lie within $\sim 0.46\text{--}0.74$ (Bliss et al. 2018; Eichler et al. 2018; Pellin et al. 2006). Considering all ejecta from model W, the isotopic ratio is ~ 0.014 if only tracers ejected at the end of the simulation are used or ~ 0.176 if also the extrapolated contribution of the outer layers is taken into account. This range of values falls far below that of the grains but is in agreement with Eichler et al. (2018) who found an integrated value of $Y(^{94}\text{Mo})/Y(^{92}\text{Mo}) \approx 0.06$ for both of their modelled CC-SNe models. However, small clumps can locally reach $Y(^{94}\text{Mo})/Y(^{92}\text{Mo}) > 0.5$ (Fig. C1) and could thus be the origin of the SiC X grains with the aforementioned ratios. Whether or not a contribution of the p/γ -process could possibly fill the gap between observations and theoretical modelling is beyond the scope of our work.

APPENDIX D: YIELD TABLES

The yield tables are given for model O, W, S, P, 35OC-Rp3, and 35OC-Rs_N in Table D1, D2, D4, D3, D6, and D5, respectively. They are separated into different contributions as outlined in Section 2.4. The contributions are given by the tracer particles, the significantly heated matter, the slightly shocked progenitor material, and the stellar wind. Furthermore, we tabulate the total extrapolated mass which is the sum of all contributions.

Table D1. Yield table for model O after 1 Gyr. The first four columns give information of the nucleus as the name, atomic number, neutron number, and mass number. The column M_I indicates the yield in M_\odot obtained from the tracer particles, M_h the yield from significantly heated matter, M_s the yield of slightly shocked progenitor material after the simulation has ended, M_w the approximated yield of the stellar wind with solar abundances according to Lodders et al. (2009), and M_e as sum of all previous yields. Nuclei with masses lower than $10^{-10}M_\odot$ for M_e are excluded from the table. The table is fully available in electronic form.

Nucleus	Z	N	A	M_I [M_\odot]	M_h [M_\odot]	M_s [M_\odot]	M_w [M_\odot]	M_e [M_\odot]
^1H	1	0	1	3.05e-04	2.95e-03	0.00e+00	4.99e+00	5.00e+00
^2H	1	1	2	1.29e-10	2.10e-09	0.00e+00	1.94e-04	1.94e-04
^3He	2	1	3	5.72e-10	6.76e-09	0.00e+00	2.40e-04	2.40e-04
^4He	2	2	4	6.47e-03	5.84e-02	3.50e-01	1.93e+00	2.34e+00
^6Li	3	3	6	0.00e+00	0.00e+00	0.00e+00	5.12e-10	5.12e-10
...								

Table D2. Same as Table D1, but for model W. The table is fully available in electronic form.

Nucleus	Z	N	A	M_I [M_\odot]	M_h [M_\odot]	M_s [M_\odot]	M_w [M_\odot]	M_e [M_\odot]
^1H	1	0	1	1.66e-03	4.58e-02	0.00e+00	4.99e+00	5.04e+00
^2H	1	1	2	4.12e-09	1.50e-07	0.00e+00	1.94e-04	1.94e-04
^3He	2	1	3	1.53e-08	5.37e-07	0.00e+00	2.40e-04	2.40e-04
^4He	2	2	4	1.55e-02	1.53e-01	3.51e-01	1.93e+00	2.45e+00
^6Li	3	3	6	0.00e+00	0.00e+00	0.00e+00	5.12e-10	5.12e-10
...								

Table D3. Same as Table D1, but for model P. The table is fully available in electronic form.

Nucleus	Z	N	A	M_I [M_\odot]	M_h [M_\odot]	M_s [M_\odot]	M_w [M_\odot]	M_e [M_\odot]
^1H	1	0	1	4.10e-05	1.81e-03	0.00e+00	4.99e+00	5.00e+00
^2H	1	1	2	9.84e-10	2.47e-07	0.00e+00	1.94e-04	1.94e-04
^3He	2	1	3	1.43e-10	1.93e-08	0.00e+00	2.40e-04	2.40e-04
^4He	2	2	4	2.40e-02	5.45e-01	3.53e-01	1.93e+00	2.85e+00
^6Li	3	3	6	0.00e+00	0.00e+00	0.00e+00	5.12e-10	5.12e-10
...								

Table D4. Same as Table D1, but for model S. The table is fully available in electronic form.

Nucleus	Z	N	A	M_I [M_\odot]	M_h [M_\odot]	M_s [M_\odot]	M_w [M_\odot]	M_e [M_\odot]
^1H	1	0	1	1.32e-07	1.50e-07	0.00e+00	4.99e+00	4.99e+00
^2H	1	1	2	0.00e+00	0.00e+00	0.00e+00	1.94e-04	1.94e-04
^3He	2	1	3	0.00e+00	0.00e+00	0.00e+00	2.40e-04	2.40e-04
^4He	2	2	4	7.29e-02	1.93e-01	3.54e-01	1.93e+00	2.55e+00
^6Li	3	3	6	0.00e+00	0.00e+00	0.00e+00	5.12e-10	5.12e-10
...								

Table D5. Same as Table D1, but for model 35OC-Rs_N. Since we did not attempt to extrapolate this model, the table contains missing values marked with a minus (see Section 2.4 for details). The table is fully available in electronic form.

Nucleus	Z	N	A	M_I [M_\odot]	M_h [M_\odot]	M_s [M_\odot]	M_w [M_\odot]	M_e [M_\odot]
^1H	1	0	1	1.12e-03	–	0.00e+00	4.99e+00	–
^2H	1	1	2	3.37e-09	–	0.00e+00	1.94e-04	–
^3He	2	1	3	6.91e-09	–	0.00e+00	2.40e-04	–
^4He	2	2	4	3.78e-02	–	3.66e-01	1.93e+00	–
^6Li	3	3	6	0.00e+00	–	0.00e+00	5.12e-10	–
...								

Table D6. Same as Table D1, but for model 35OC-Rp3. The table is fully available in electronic form.

Nucleus	Z	N	A	$M_l [M_\odot]$	$M_h [M_\odot]$	$M_s [M_\odot]$	$M_w [M_\odot]$	$M_e [M_\odot]$
^1H	1	0	1	1.62e-03	8.16e-04	0.00e+00	4.99e+00	5.00e+00
^2H	1	1	2	3.43e-10	8.98e-11	0.00e+00	1.94e-04	1.94e-04
^3He	2	1	3	1.30e-09	2.57e-10	0.00e+00	2.40e-04	2.40e-04
^4He	2	2	4	1.52e-01	1.80e+00	2.99e-01	1.93e+00	4.17e+00
^6Li	3	3	6	0.00e+00	0.00e+00	0.00e+00	5.12e-10	5.12e-10
...								

This paper has been typeset from a $\text{\TeX}/\text{\LaTeX}$ file prepared by the author.

List of astronomical key words (Updated on 2020 January)

This list is common to *Monthly Notices of the Royal Astronomical Society*, *Astronomy and Astrophysics*, and *The Astrophysical Journal*. In order to ease the search, the key words are subdivided into broad categories. No more than *six* subcategories altogether should be listed for a paper.

The subcategories in boldface containing the word ‘individual’ are intended for use with specific astronomical objects; these should never be used alone, but always in combination with the most common names for the astronomical objects in question. Note that each object counts as one subcategory within the allowed limit of six.

The parts of the key words in italics are for reference only and should be omitted when the keywords are entered on the manuscript.

General

editorials, notices
errata, addenda
extraterrestrial intelligence
history and philosophy of astronomy
miscellaneous
obituaries, biographies
publications, bibliography
sociology of astronomy
standards

Physical data and processes

acceleration of particles
accretion, accretion discs
asteroseismology
astrobiology
astrochemistry
astroparticle physics
atomic data
atomic processes
black hole physics
chaos
conduction
convection
dense matter
diffusion
dynamo
elementary particles
equation of state
gravitation
gravitational lensing: micro
gravitational lensing: strong
gravitational lensing: weak
gravitational waves
hydrodynamics
instabilities
line: formation
line: identification
line: profiles
magnetic fields
magnetic reconnection
(*magnetohydrodynamics*) MHD
masers
molecular data
molecular processes
neutrinos
nuclear reactions, nucleosynthesis, abundances
opacity
plasmas
polarization

radiation: dynamics
radiation mechanisms: general
radiation mechanisms: non-thermal
radiation mechanisms: thermal
radiative transfer
relativistic processes
scattering
shock waves
solid state: refractory
solid state: volatile
turbulence
waves

Astronomical instrumentation, methods and techniques

atmospheric effects
balloons
instrumentation: adaptive optics
instrumentation: detectors
instrumentation: high angular resolution
instrumentation: interferometers
instrumentation: miscellaneous
instrumentation: photometers
instrumentation: polarimeters
instrumentation: spectrographs
light pollution
methods: analytical
methods: data analysis
methods: laboratory: atomic
methods: laboratory: molecular
methods: laboratory: solid state
methods: miscellaneous
methods: numerical
methods: observational
methods: statistical
site testing
space vehicles
space vehicles: instruments
techniques: high angular resolution
techniques: image processing
techniques: imaging spectroscopy
techniques: interferometric
techniques: miscellaneous
techniques: photometric
techniques: polarimetric
techniques: radar astronomy
techniques: radial velocities
techniques: spectroscopic
telescopes

Astronomical data bases

astronomical data bases: miscellaneous
atlases
catalogues
surveys
virtual observatory tools

Software

software: data analysis
software: development
software: documentation
software: public release
software: simulations

Astrometry and celestial mechanics

astrometry
celestial mechanics
eclipses
ephemerides
occultations
parallaxes
proper motions
reference systems
time

The Sun

Sun: abundances
Sun: activity
Sun: atmosphere
Sun: chromosphere
Sun: corona
Sun: coronal mass ejections (CMEs)
Sun: evolution
Sun: faculae, plages
Sun: filaments, prominences
Sun: flares
Sun: fundamental parameters
Sun: general
Sun: granulation
Sun: helioseismology
Sun: heliosphere
Sun: infrared
Sun: interior
Sun: magnetic fields
Sun: oscillations
Sun: particle emission
Sun: photosphere
Sun: radio radiation
Sun: rotation
(*Sun*;) solar–terrestrial relations
(*Sun*;) solar wind
(*Sun*;) sunspots
Sun: transition region
Sun: UV radiation
Sun: X-rays, gamma-rays

Planetary systems

comets: general

comets: individual: . . .

Earth
interplanetary medium
Kuiper belt: general

Kuiper belt objects: individual: . . .

meteorites, meteors, meteoroids

minor planets, asteroids: general

minor planets, asteroids: individual: . . .

Moon
Oort Cloud
planets and satellites: atmospheres
planets and satellites: aurorae
planets and satellites: composition
planets and satellites: detection
planets and satellites: dynamical evolution and stability
planets and satellites: formation
planets and satellites: fundamental parameters
planets and satellites: gaseous planets
planets and satellites: general

planets and satellites: individual: . . .

planets and satellites: interiors
planets and satellites: magnetic fields
planets and satellites: oceans
planets and satellites: physical evolution
planets and satellites: rings
planets and satellites: surfaces
planets and satellites: tectonics
planets and satellites: terrestrial planets
planet–disc interactions
planet–star interactions
protoplanetary discs
zodiacal dust

Stars

stars: abundances
stars: activity
stars: AGB and post-AGB
stars: atmospheres
(*stars*;) binaries (*including multiple*): close
(*stars*;) binaries: eclipsing
(*stars*;) binaries: general
(*stars*;) binaries: spectroscopic
(*stars*;) binaries: symbiotic
(*stars*;) binaries: visual
stars: black holes
(*stars*;) blue stragglers
(*stars*;) brown dwarfs
stars: carbon
stars: chemically peculiar
stars: chromospheres
(*stars*;) circumstellar matter
stars: coronae
stars: distances
stars: dwarf novae
stars: early-type
stars: emission-line, Be
stars: evolution
stars: flare
stars: formation
stars: fundamental parameters
(*stars*;) gamma-ray burst: general
(*stars*;) **gamma-ray burst: individual: . . .**
stars: general
(*stars*;) Hertzsprung–Russell and colour–magnitude diagrams
stars: horizontal branch
stars: imaging
stars: individual: . . .
stars: interiors

- stars: jets
- stars: kinematics and dynamics
- stars: late-type
- stars: low-mass
- stars: luminosity function, mass function
- stars: magnetars
- stars: magnetic fields
- stars: massive
- stars: mass-loss
- stars: neutron
- (stars:) novae, cataclysmic variables
- stars: oscillations (*including pulsations*)
- stars: peculiar (*except chemically peculiar*)
- (stars:) planetary systems
- stars: Population II
- stars: Population III
- stars: pre-main-sequence
- stars: protostars
- (stars:) pulsars: general
- (stars:) **pulsars: individual: . . .**
- stars: rotation
- stars: solar-type
- (stars:) starspots
- stars: statistics
- (stars:) subdwarfs
- (stars:) supergiants
- (stars:) supernovae: general
- (stars:) **supernovae: individual: . . .**
- stars: variables: Cepheids
- stars: variables: Scuti
- stars: variables: general
- stars: variables: RR Lyrae
- stars: variables: S Doradus
- stars: variables: T Tauri, Herbig Ae/Be
- (stars:) white dwarfs
- stars: winds, outflows
- stars: Wolf–Rayet

Interstellar medium (ISM), nebulae

- ISM: abundances
- ISM: atoms
- ISM: bubbles
- ISM: clouds
- (ISM:) cosmic rays
- (ISM:) dust, extinction
- ISM: evolution
- ISM: general
- (ISM:) HII regions
- (ISM:) Herbig–Haro objects

ISM: individual objects: . . .

- (*except planetary nebulae*)
- ISM: jets and outflows
- ISM: kinematics and dynamics
- ISM: lines and bands
- ISM: magnetic fields
- ISM: molecules
- (ISM:) photodissociation region (PDR)
- (ISM:) planetary nebulae: general
- (ISM:) **planetary nebulae: individual: . . .**
- ISM: structure
- ISM: supernova remnants

The Galaxy

- Galaxy: abundances
- Galaxy: bulge
- Galaxy: centre
- Galaxy: disc
- Galaxy: evolution
- Galaxy: formation
- Galaxy: fundamental parameters
- Galaxy: general
- (Galaxy:) globular clusters: general
- (Galaxy:) **globular clusters: individual: . . .**
- Galaxy: halo
- Galaxy: kinematics and dynamics
- (Galaxy:) local interstellar matter
- Galaxy: nucleus
- (Galaxy:) open clusters and associations: general
- (Galaxy:) **open clusters and associations: individual: . . .**
- (Galaxy:) solar neighbourhood
- Galaxy: stellar content
- Galaxy: structure

Galaxies

- galaxies: abundances
- galaxies: active
- galaxies: bar
- (galaxies:) BL Lacertae objects: general
- (galaxies:) **BL Lacertae objects: individual: . . .**
- galaxies: bulges
- galaxies: clusters: general

galaxies: clusters: individual: . . .

- galaxies: clusters: intracluster medium
- galaxies: disc
- galaxies: distances and redshifts
- galaxies: dwarf
- galaxies: elliptical and lenticular, cD
- galaxies: evolution
- galaxies: formation
- galaxies: fundamental parameters
- galaxies: general
- galaxies: groups: general

galaxies: groups: individual: . . .

- galaxies: haloes
- galaxies: high-redshift

galaxies: individual: . . .

- galaxies: interactions
- (galaxies:) intergalactic medium
- galaxies: irregular
- galaxies: ISM
- galaxies: jets
- galaxies: kinematics and dynamics
- (galaxies:) Local Group
- galaxies: luminosity function, mass function
- (galaxies:) Magellanic Clouds
- galaxies: magnetic fields
- galaxies: nuclei
- galaxies: peculiar
- galaxies: photometry
- (galaxies:) quasars: absorption lines
- (galaxies:) quasars: emission lines
- (galaxies:) quasars: general

(galaxies:) **quasars: individual: . . .**
(galaxies:) quasars: supermassive black holes
galaxies: Seyfert
galaxies: spiral
galaxies: starburst
galaxies: star clusters: general

galaxies: star clusters: individual: . . .
galaxies: star formation
galaxies: statistics
galaxies: stellar content
galaxies: structure

Cosmology

(cosmology:) cosmic background radiation
(cosmology:) cosmological parameters
(cosmology:) dark ages, reionization, first stars
(cosmology:) dark energy
(cosmology:) dark matter
(cosmology:) diffuse radiation
(cosmology:) distance scale
(cosmology:) early Universe
(cosmology:) inflation
(cosmology:) large-scale structure of Universe
cosmology: miscellaneous
cosmology: observations
(cosmology:) primordial nucleosynthesis
cosmology: theory

Resolved and unresolved sources as a function of wavelength

gamma-rays: diffuse background
gamma-rays: galaxies
gamma-rays: galaxies: clusters
gamma-rays: general
gamma-rays: ISM
gamma-rays: stars
infrared: diffuse background
infrared: galaxies
infrared: general
infrared: ISM
infrared: planetary systems
infrared: stars
radio continuum: galaxies
radio continuum: general
radio continuum: ISM
radio continuum: planetary systems
radio continuum: stars
radio continuum: transients
radio lines: galaxies
radio lines: general
radio lines: ISM
radio lines: planetary systems
radio lines: stars
submillimetre: diffuse background
submillimetre: galaxies
submillimetre: general
submillimetre: ISM
submillimetre: planetary systems
submillimetre: stars
ultraviolet: galaxies

ultraviolet: general
ultraviolet: ISM
ultraviolet: planetary systems
ultraviolet: stars
X-rays: binaries
X-rays: bursts
X-rays: diffuse background
X-rays: galaxies
X-rays: galaxies: clusters
X-rays: general
X-rays: individual: . . .
X-rays: ISM
X-rays: stars

Transients

(transients:) black hole mergers
(transients:) black hole - neutron star mergers
(transients:) fast radio bursts
(transients:) gamma-ray bursts
(transients:) neutron star mergers
transients: novae
transients: supernovae
transients: tidal disruption events